AGU ADVANCING EARTH AND SPACE SCIENCES

JGR Solid Earth

RESEARCH ARTICLE
10.1029/2024JB028846

Rapid Ductile Strain Localization Due To Thermal Runaway

A. Spang[1], M. Thielmann[1,2], and D. Kiss[3,4]

[1]Bayerisches Geoinstitut, Universität Bayreuth, Bayreuth, Germany, [2]Institut für Geowissenschaften, Christian-Albrechts-Universität Kiel, Kiel, Germany, [3]Institut für Geowissenschaften, Johannes Gutenberg-Universität Mainz, Mainz, Germany, [4]Department of Reservoir Technology, Institute for Energy Technology, Kjeller, Norway

Key Points:

- Numerical investigation of thermal runaway in visco-elastic material with diffusion creep, dislocation creep and low-temperature plasticity
- Nondimensional scaling analysis reveals two dimensionless groups governing the occurrence of thermal runaway
- Ductile localization can cause slip events in line with deep earthquakes and pseudotachylyte formation at subducting slab core conditions

Supporting Information:

Supporting Information may be found in the online version of this article.

Correspondence to:

A. Spang,
arne.spang@uni-bayreuth.de

Citation:

Spang, A., Thielmann, M., & Kiss, D. (2024). Rapid ductile strain localization due to thermal runaway. *Journal of Geophysical Research: Solid Earth*, *129*, e2024JB028846. https://doi.org/10.1029/2024JB028846

Received 2 FEB 2024
Accepted 16 SEP 2024

Author Contributions:

Conceptualization: A. Spang, M. Thielmann
Data curation: A. Spang
Formal analysis: A. Spang
Funding acquisition: M. Thielmann
Investigation: A. Spang
Methodology: A. Spang, M. Thielmann, D. Kiss
Project administration: M. Thielmann
Resources: M. Thielmann
Software: A. Spang, M. Thielmann, D. Kiss
Supervision: M. Thielmann
Validation: A. Spang
Visualization: A. Spang
Writing – original draft: A. Spang

Abstract Thermal runaway is a ductile localization mechanism that has been linked to deep-focus earthquakes and pseudotachylyte formation. In this study, we investigate the dynamics of this process using one-dimensional, numerical models of simple shear deformation. The models employ a visco-elastic rheology where viscous creep is accommodated with a composite rheology encompassing diffusion and dislocation creep as well as low-temperature plasticity. To solve the nonlinear system of differential equations governing this rheology, we utilize the pseudo-transient iterative method in combination with a viscosity regularization to avoid resolution dependencies. To determine the impact of different model parameters on the occurrence of thermal runaway, we perform a parameter sensitivity study consisting of 6,000 numerical experiments. We observe two distinct behaviors, namely a stable regime, characterized by transient shear zone formation accompanied by a moderate (100–300 K) temperature increase, and a thermal runaway regime, characterized by strong localization, rapid slip and a temperature surge of thousands of Kelvin. Nondimensional scaling analysis allows us to determine two dimensionless groups that predict the model behavior. The ratio t_r/t_d represents the competition between heat generation from stress relaxation and heat loss due to thermal diffusion while the ratio U_{el}/U_{th} compares the stored elastic energy to thermal energy in the system. Thermal runaway occurs if t_r/t_d is small and U_{el}/U_{th} is large. Our results demonstrate that thermal runaway is a viable mechanism driving fast slip events that are in line with deep-focus earthquakes and pseudotachylyte formation at conditions resembling cores of subducting slabs.

Plain Language Summary Thermal runaway is a mechanism that concentrates material deformation into thin layers without breaking the material and has been linked to earthquakes more than 70 km below the surface. This study uses one-dimensional computer models with a complex material behavior and conducts 6,000 numerical experiments to investigate the influence of different parameters like temperature, deformation rate and material properties. Results show two distinct behaviors, namely a stable regime with slow sliding and a temperature rise of 100–300 K or thermal runaway with fast movement and a temperature increase of a few thousand Kelvin. We find two dimensionless ratios that are combinations of the input parameters and can predict the behavior. The ratio t_r/t_d compares heat production to heat loss, and the ratio U_{el}/U_{th} compares stored elastic energy to thermal energy. If the first ratio is small and the second ratio is large, thermal runaway occurs. Our results show that thermal runaway could cause fast deformation events like earthquakes and produce thin layers of molten rock in conditions that are typical for subducting plates.

1. Introduction

Strain localization characterizes geodynamic processes across scales ranging from μm (mineral grains) to thousands of km (plate tectonics) by allowing "stiff" blocks to move past each other on thin, "weak" layers. In the crust, this usually occurs via brittle failure (i.e., breaking the rock). As brittle strength is expected to increase linearly with confining pressure (Byerlee, 1978) until reaching the strength of atomic bonds (Renshaw & Schulson, 2007), a ductile localization process is likely dominant at larger depths. However, ductile rheologies such as Newtonian or non-Newtonian viscous flow usually do not localize deformation unless self-weakening feedback mechanisms are active (Bercovici & Karato, 2002).

Nevertheless, from the occurrence of intermediate-depth and deep-focus earthquakes (70–300 km and 300–700 km depth respectively), we do know that deformation at depth may be strongly localized in both space and time (Leith & Sharpe, 1936; Turner, 1922; Wadati, 1928). These deep earthquakes are not only distinct from shallow earthquakes with respect to their depths, but often also exhibit higher stress drops (Frohlich, 1989), low aftershock frequencies (Green & Houston, 1995; Kagan & Knopoff, 1980) and low energy radiation efficiencies

Writing – review & editing: A. Spang, M. Thielmann, D. Kiss

(Houston, 2015; Kanamori et al., 1998). These low radiation efficiencies imply that a large amount of energy was dissipated during rupture, which has been interpreted as indicator for non-brittle rupture mechanisms (Tibi et al., 2003; Venkataraman & Kanamori, 2004).

Three main mechanisms have been proposed to govern deep earthquake nucleation and rupture: dehydration embrittlement, transformational faulting and thermal runaway (e.g., Frohlich, 1989; Houston, 2015; Zhan, 2020), with the first one being related to brittle failure and the other two to ductile localization. Dehydration embrittlement due to the release of fluids from metamorphic reactions (e.g., Hacker et al., 2003; Meade & Jeanloz, 1991; Raleigh & Paterson, 1965) has mainly been invoked to explain intermediate-depth earthquakes. Deep-focus earthquakes are commonly associated with transformational faulting due to the transformation of metastable olivine to wadsleyite or ringwoodite (e.g., Burnley et al., 1991; Gasc et al., 2022; Green & Burnley, 1989; Kirby, 1987; Kirby et al., 1996; Schubnel et al., 2013; Wang et al., 2017). During this phase transition, it is thought that fine-grained (and hence weak) lenses are formed which ultimately connect to form a weak layer where deformation can localize (Tingle et al., 1993).

Finally, viscous dissipation has been proposed as a potential failure mechanism for both intermediate-depth and deep-focus earthquakes (Deseta et al., 2014; Hobbs et al., 1986; John et al., 2009; Kelemen & Hirth, 2007; Ogawa, 1987; Ohuchi et al., 2017; Prieto et al., 2013; Thielmann, 2018; Thielmann et al., 2015; Tresca, 1878). The combination of deformation, shear heating and a temperature-dependent rheology forms a positive feedback loop called thermal runaway that can lead to catastrophic strain localization and fast-slip events (Gruntfest, 1963). Theoretical considerations have shown that this mechanism requires stresses on the order of 1 GPa (Braeck & Podladchikov, 2007). Such stresses may be generated by dehydration-driven stress transfer (Ferrand et al., 2017), stress amplifications around weak inclusions (Toffol et al., 2022), dehydration embrittlement or transformational faulting. This dual-mechanism process has been proposed to explain the occurrence of deep-focus earthquakes outside of the metastable olivine wedge (e.g., Bezada & Humphreys, 2012; McGuire et al., 1997; Zhan, 2020).

Ductile localization has also been investigated as the cause of lithospheric-scale shear zones. Proposed mechanisms include grain size reduction (e.g., Bercovici & Ricard, 2012; Braun et al., 1999; Foley, 2018; Kameyama et al., 1997; Ricard & Bercovici, 2009; Thielmann et al., 2015), metamorphic reactions caused by fluid infiltration (e.g., Barnes et al., 2004; Getsinger et al., 2013; Jamtveit et al., 2016) and viscous dissipation (e.g., Brinkman, 1951; Regenauer-Lieb & Yuen, 1998; Yuen et al., 1978). Several studies have shown that shear heating has a strong impact on lithospheric deformation (e.g., Kaus & Podladchikov, 2006; Kiss et al., 2019; Regenauer-Lieb & Yuen, 2004; Schmalholz & Duretz, 2015; Thielmann & Kaus, 2012).

A number of previous one-dimensional (1D) studies have numerically investigated ductile localization due to viscous dissipation with varying rheological complexity ranging from diffusion creep to nonlinear visco-elasticity including grain size evolution (e.g., Braeck et al., 2009; Braun et al., 1999; Kaus & Podladchikov, 2006; Kelemen & Hirth, 2007; Ogawa, 1987; Thielmann et al., 2015; Yuen et al., 1978). Kameyama et al. (1999); Kelemen and Hirth (2007); Thielmann (2018) are the only studies to include low-temperature plasticity (LTP) in their rheological model, concluding that it inhibits or delays thermal runaway at natural conditions. While all studies observe ductile localization, an important distinction can be made between localization onto finite width shear zones accompanied by moderate temperature increases (100–300 K) toward a quasi-steady-state (e.g., Kiss et al., 2019; Yuen et al., 1978) and infinite-like localization accompanied by temperature increases of several hundreds or thousands of Kelvin within seconds (e.g., Braeck et al., 2009; Ogawa, 1987). We will only refer to the latter case as thermal runaway. While successful two- and three-dimensional (2D and 3D) models of ductile localization exist (e.g., Duretz et al., 2019; Kaus & Podladchikov, 2006; Kiss et al., 2019), extensive parameter studies are limited to 1D due to the large computational cost of 2D and 3D simulations.

The aims of our study are as follows: (a) develop a 1D numerical code that can cover the loading, heating and unloading (through shear zones and/or thermal runaway) of rock with a rheology including elasticity, diffusion creep, dislocation creep and LTP, (b) present numerical strategies to deal with nonlinearities during thermal runaway, (c) illustrate the effects of such strategies, (d) identify the necessary conditions for thermal runaway in velocity-driven simple shear.

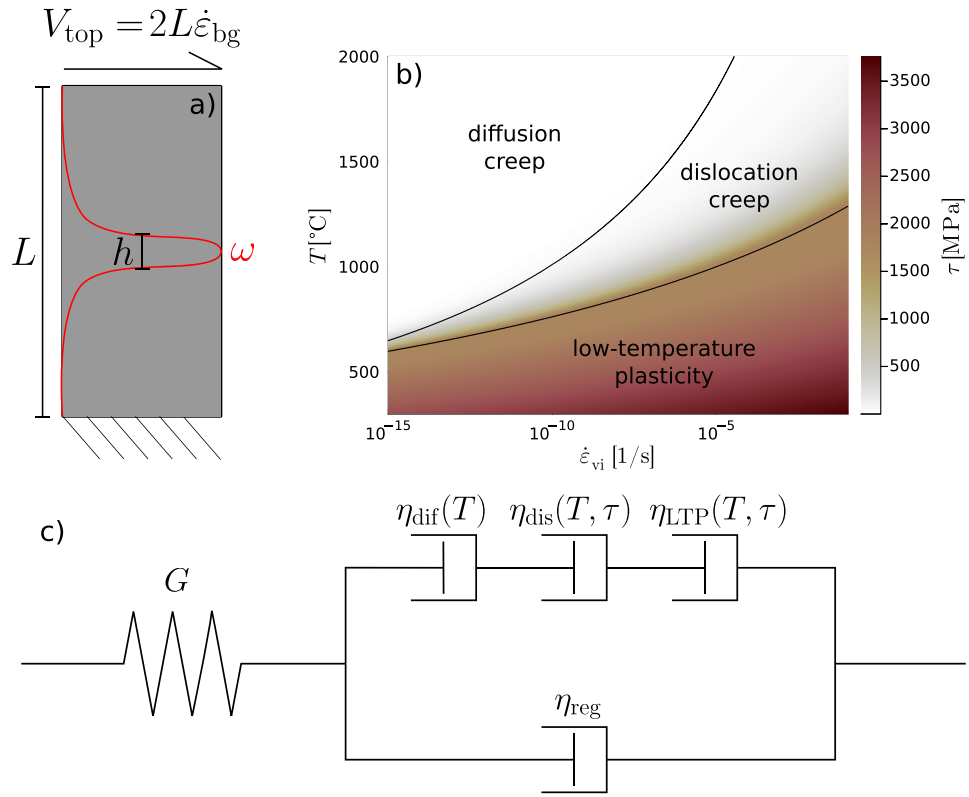

Figure 1. Model setup and rheology. (a) 1D Model setup including boundary conditions. Note that the model only has one cell and no spatial extent in the horizontal direction. h and L are not to scale. (b) Deformation mechanism map for our rheological model. (c) Illustration of the individual components of the rheological model. η_{reg} is purely numerical and facilitates stability during the runaway when the upper viscosity branch trends toward 0.

2. Methods

Section 2.1 presents the model setup, Section 2.2 lists the governing equations and Section 2.3 outlines their implementation. Section 2.4 outlines the ranges of our parameter study.

2.1. Model Setup

We use a 1D simple shear setup with an olivine rheology, a central, weak anomaly and constant kinematic boundary conditions that load the model (Figure 1a). The anomaly is created by multiplying the diffusion and dislocation creep flow law pre-factors by a vector ω which follows a normal distribution, centered at 0, with a minimum of 1, a maximum of $\omega_0 > 1$ and a full-width-half-maximum (FWHM) of h:

$$\omega = 1 + (\omega_0 - 1)\, e^{-\frac{1}{2}\left(\frac{x}{\sigma}\right)^2}, \tag{1}$$

where

$$\sigma = \frac{h}{\sqrt{8\ln(2)}}, \tag{2}$$

and x is the coordinate vector. The lower domain boundary is no-slip and the upper edge is moving with a fixed velocity of

$$V_{top} = 2L\dot{\varepsilon}_{bg}, \tag{3}$$

where V_{top} is the imposed boundary velocity, L is the size of the domain and $\dot{\varepsilon}_{bg}$ is the background strain rate. Both boundaries are thermally insulated (i.e., no heat flux).

2.2. Governing Equations

The system described above is governed by the equations.

$$\frac{\partial \tau}{\partial x} = 0, \tag{4}$$

$$\rho C_p \frac{dT}{dt} = \lambda \frac{\partial^2 T}{\partial x^2} + \tau \dot{\varepsilon}_{vi}, \tag{5}$$

$$\dot{\varepsilon} = \frac{1}{2}\frac{\partial V}{\partial x}, \tag{6}$$

where τ is the shear stress (xy-component of the Cauchy stress deviator), x is the spatial dimension, ρ the density, C_p the specific heat capacity, T the temperature, t the time, λ the thermal conductivity, $\dot{\varepsilon}$ the shear component (analogously to τ) of the deviatoric strain rate, $\dot{\varepsilon}_{vi}$ its viscous part and V the velocity perpendicular to the spatial dimension. All other components of the stress and strain rate tensor and velocity vector are equal to zero. This implies that the divergence of velocity is zero and the system incompressible. For simplicity, we neglect inertia and body forces (i.e., gravity) as well as adiabatic and radiogenic heating. The last term of Equation 5 represents heat generation by viscous dissipation.

We describe the visco-elastic rheology via a Maxwell model:

$$\dot{\varepsilon} = \dot{\varepsilon}_{el} + \dot{\varepsilon}_{vi} = \frac{1}{2G}\frac{d\tau}{dt} + \frac{\tau}{2\eta}, \tag{7}$$

where $\dot{\varepsilon}_{el}$ and $\dot{\varepsilon}_{vi}$ are the elastic and viscous components of the deviatoric strain rate, G the shear modulus and η the effective viscosity. Equation 7 ensures that elastic deformation dominates at small time scales and viscous deformation dominates at large stresses.

2.3. Implementation

We discretize Equations 4–7 with finite differences on a staggered grid where material parameters, pressure, temperature, stress and strain rate are defined on cell centers and velocities on cell edges (e.g., Gerya & Yuen, 2003). Equations are solved using the damped pseudo-transient approach (e.g., Duretz et al., 2019; Frankel, 1950; Räss et al., 2022). The code is written in the Julia programming language and we utilize the package GeoParams.jl (Kaus et al., 2023) for internal nondimensionalization and scaling.

2.3.1. Pseudo-Transient Approach

In the pseudo-transient approach, the conservation equations are solved at every physical time step by introducing a residual (or pseudo time derivative) for each equation and iteratively incrementing the primary variables V and T until the residuals are smaller than a given numerical tolerance. Applying this procedure to Equations 4 and 5 yields.

$$\frac{\partial V}{\partial \psi} = \frac{\partial \tau}{\partial x}, \tag{8}$$

$$\frac{\partial T}{\partial \psi} = \frac{\lambda \frac{\partial^2 T}{\partial x^2} + \tau\, \dot{\varepsilon}_{vi}}{\rho C_p} - \frac{dT}{dt}, \tag{9}$$

where $\frac{\partial}{\partial \psi}$ denotes the residual or evolution in pseudo-time. During each pseudo-time iteration, each primary variable is incremented proportional to the sum of the current residual and the previous increment (Duretz et al., 2019):

$$\Delta_\gamma = \left[\frac{\partial \gamma}{\partial \psi} + \left(1 - \frac{1}{\zeta_\gamma}\right)\Delta_\gamma^{\text{prev}}\right]\Delta\psi_\gamma, \tag{10}$$

where γ is either V or T, Δ_γ is the increment to the respective variable, $\Delta_\gamma^{\text{prev}}$ is the increment of the previous iteration, ζ_γ is the damping parameter (>1) and $\Delta\psi_\gamma$ is the size of the pseudo time step.

2.3.2. Rheology and Density

Viscous deformation is a combination of diffusion creep, dislocation creep and LTP:

$$\dot{\varepsilon}_{\text{vi}} = \dot{\varepsilon}_{\text{dif}} + \dot{\varepsilon}_{\text{dis}} + \dot{\varepsilon}_{\text{LTP}}, \tag{11}$$

where the subscripts$_{\text{dif,dis}}$ and $_{\text{LTP}}$ denote diffusion creep, dislocation creep and LTP respectively. Consequently, the effective viscosity η can be expressed as

$$\eta = \left(\frac{1}{\eta_{\text{dif}}} + \frac{1}{\eta_{\text{dis}}} + \frac{1}{\eta_{\text{LTP}}}\right)^{-1}, \tag{12}$$

$$\eta_{\text{dif}} = \frac{1}{2}A_{\text{dif}}^{-1}\, d^m\, e^{\frac{E_{\text{dif}}}{RT}}, \tag{13}$$

$$\eta_{\text{dis}} = \frac{1}{2}(A_{\text{dis}})^{-\frac{1}{n}}\left(\dot{\varepsilon}_{\text{dis}}\right)^{\frac{1}{n}-1} e^{\frac{E_{\text{dis}}}{nRT}}, \tag{14}$$

$$\eta_{\text{LTP}} = \frac{\sigma_{\text{LTP}}}{2\,\dot{\varepsilon}_{\text{LTP}}}, \tag{15}$$

where A are pre-factors and E are activation energies of the respective flow laws, d is the grain size, m the grain size exponent of diffusion creep, R the universal gas constant and n the powerlaw exponent of dislocation creep. The LTP-stress σ_{LTP} is given by

$$\sigma_{\text{LTP}} = \frac{R\,T}{E_{\text{LTP}}}\,\sigma_{\text{res}}\;\sinh^{-1}\left(\frac{\dot{\varepsilon}_{\text{LTP}}}{A_{\text{LTP}}}e^{\frac{E_{\text{LTP}}}{RT}}\right) + \sigma_{\text{b}}, \tag{16}$$

$$\sigma_{\text{res}} = \sigma_{\text{L}} + \frac{\sigma_{\text{K}}}{\sqrt{d}}, \tag{17}$$

where σ_{b} is the back stress which describes the effect of long-range interactions of dislocations. σ_{L} is lattice friction and combines with the material constant σ_{K} and the grain size to describe local resistance to dislocation motion (σ_{res}) (Hansen et al., 2019). Given the nonlinear nature of dislocation creep and LTP, the strain rate partitioning (Equation 11) can not be solved analytically, but requires an iterative approach. It can be updated and solved alongside the conservation Equations 8 and 9. Once the left hand side terms in Equations 8 and 9, as well as the residual of Equation 11 are smaller than the tolerance, the solution is converged and is equivalent to a fully implicit, backward Euler solution with converged non-linearities.

Figure 1b shows a deformation mechanism map for the rheological model described by Equations 11–17 and illustrates that LTP dominates at low temperatures, diffusion creep at high temperatures and dislocation creep at high strain rates due its shear thinning nature. The values of all used material parameters are given by Table 1.

As we are focused on understanding the impact of the composite creep rheology, we do not include grain size evolution in our model. In addition, there is no experimental data on the contribution of LTP to grain size evolution. Even for dislocation creep, the partitioning factor of dissipative work is a controversial topic spanning several orders of magnitude in different studies (Austin et al., 2008; Chrysochoos & Belmahjoub, 1992; Holtzman et al., 2018; Mulyukova & Bercovici, 2017; Rozel et al., 2011; Ruh et al., 2022).

Table 1
Material Parameters

Parameter		Value
G	[GPa]	40–160 (80)
m		3
A_{dif}	$[\mu m^m\ MPa^{-1}\ s^{-1}]$	1.5×10^9
E_{dif}	$[kJ\ mol^{-1}]$	375
d	[μm]	100
n		3.5
A_{dis}	$[MPa^{-n}\ s^{-1}]$	1.1×10^5
E_{dis}	$[kJ\ mol^{-1}]$	530
A_{LTP}	$[s^{-1}]$	5×10^{20}
E_{LTP}	$[kJ\ mol^{-1}]$	550
σ_L	[GPa]	3.1
σ_K	$[GPa\ \mu m^{0.5}]$	3.2
σ_b	[GPa]	0.9–2.7 (1.8)
P_0	[GPa]	10
ρ_0	$[kg\ m^{-3}]$	3,300
ν		0.25
C_p	$[J\ kg^{-1}\ K^{-1}]$	1,000
λ	$[J\ s^{-1}\ m^{-1}\ K^{-1}]$	0.75–12 (3)

Note. Diffusion and dislocation creep are for dry olivine from Hirth and Kohlstedt (2003) and low-temperature plasticity from Hansen et al. (2019). Values with ranges were varied with the default value in parenthesis.

We assume a background pressure $P_0 = 10$ GPa which is roughly equivalent to 300 km depth and a Poisson's ratio of $\nu = 0.25$ to adjust density (ρ) to upper mantle conditions.

$$\rho = \rho_0\, e^{\frac{P_0}{K_b}}, \tag{18}$$

$$K_b = \frac{2\,G\,(1+\nu)}{3\,(1-2\,\nu)}. \tag{19}$$

2.3.3. Regularization

Once initiated, the feedback loop of thermal runaway has no self-limiting mechanism other than heat diffusion. In viscous models, thermal diffusion can limit localization to a finite width (Duretz et al., 2014; Kiss et al., 2019). However, for visco-elastic rheologies, deformation commonly localizes onto a single grid cell which leads to mesh-dependent results (e.g., De Borst et al., 1993; Iordache & Willam, 1998; Jacquey et al., 2021) and temperatures of several tens of thousands °C (e.g., Ogawa, 1987; Thielmann et al., 2015). This poses several challenges: (a) The temperature rise is unrealistic as it would naturally be inhibited by melting. (b) Computed velocities depend on spatial resolution. (c) The solution is numerically unstable as Equation 12 approaches zero at high temperatures.

To deal with the aforementioned issues, we regularize the viscous components of our rheological model (Figure 1c), effectively adding a term to Equation 12 which yields

$$\eta = \left(\frac{1}{\eta_{dif}} + \frac{1}{\eta_{dis}} + \frac{1}{\eta_{LTP}}\right)^{-1} + \eta_{reg}. \tag{20}$$

This approach has also been used to regularize brittle plasticity (e.g., Duretz et al., 2020; Jacquey & Cacace, 2020; Kiss et al., 2023) and rate-and-state friction (e.g., Goudarzi et al., 2023; Pranger et al., 2022). In Section 3.2, we demonstrate how η_{reg} affects stress evolution, maximum velocity and maximum temperature. We furthermore show how it introduces a grid independent length scale into the thickness of the shear zone.

2.3.4. Discretization

During thermal runaway, temperature, stress and velocity change drastically, thus requiring physical time steps in the range of milliseconds. The loading phase does, however, require time steps of hundreds of years. To address this issue, we employ an adaptive time-stepping scheme which adjusts the physical time step depending on the maximum temperature and stress change in the model. To maximize the resolution in the area where runaway is expected, we employ a variable grid spacing where the central quarter of cells are identical in size, and cell size linearly increases toward the outside. For the parameter study, central cells have a size of 1 m and the outermost cells are 125 m wide.

2.4. Parameter Study

We conduct 6,000 numerical experiments, varying the parameters $\dot{\varepsilon}_{bg}$, G, σ_b, L, λ, T_0, ω_0 and h/L to identify under which conditions thermal runaway occurs. $\dot{\varepsilon}_{bg}$ and T_0 have been established to be critical parameters by the majority of previous studies. We also vary G and L as they control the amount of stored elastic energy that can be released by runaway. λ is critical as it characterizes thermal diffusion which competes with shear heating. ω_0 and h/L describe the perturbation and are usually chosen arbitrarily. So investigating their role is also important. Finally, σ_b is the most influential parameter in LTP, the least constrained component of our composite rheology. As every additional free parameter significantly increases the number of necessary models, we do not vary the well-established (Hirth & Kohlstedt, 2003) parameters for diffusion and dislocation creep. We present a smaller, separate parameter study for those parameters in Text S1 in Supporting Information S1.

Table 2
Model Parameter Ranges

	$\dot{\varepsilon}_{bg}$ [s^{-1}]	G [GPa]	σ_b [GPa]	L [km]	λ [J s^{-1} m^{-1} K^{-1}]	T_0 [°C]	ω_0	h/L
Min	1×10^{-14}	40	0.9	1	0.75	550	1.01	0.005
Max	5×10^{-12}	160	2.7	180	12	750	100	0.080

The range for each parameter is given in Table 2. Temperatures are typical for the cores of subducting slabs (e.g., Gasc et al., 2022; Kirby et al., 1996). Simulations run until a shear strain of 1 which equates to a simulation time of 6–3,000 kyr depending on $\dot{\varepsilon}_{bg}$. All models use $\eta_{reg} = 10^{12}$ Pa s as this introduces no significant changes in the stress evolution, while improving convergence (see Section 3.2). In electronic supplementary Table S3, we show the full list of input parameter combinations.

3. Results

3.1. General Behavior

In Figure 2, we show the temporal evolution of stress and maximum temperature in four representative simulations. Some models exhibit LTP and thermal runaway (Figure 2a), some show runaway without LTP (Figure 2b), some exhibit LTP without runaway (Figure 2c) and other simulations exhibit neither process (Figure 2d). Each model starts with a phase of elastic loading where stress increases linearly until viscous creep limits and/or releases it. If models reach the LTP limit σ_{LTP} (Figures 2a and 2c), the temperature then starts to rise

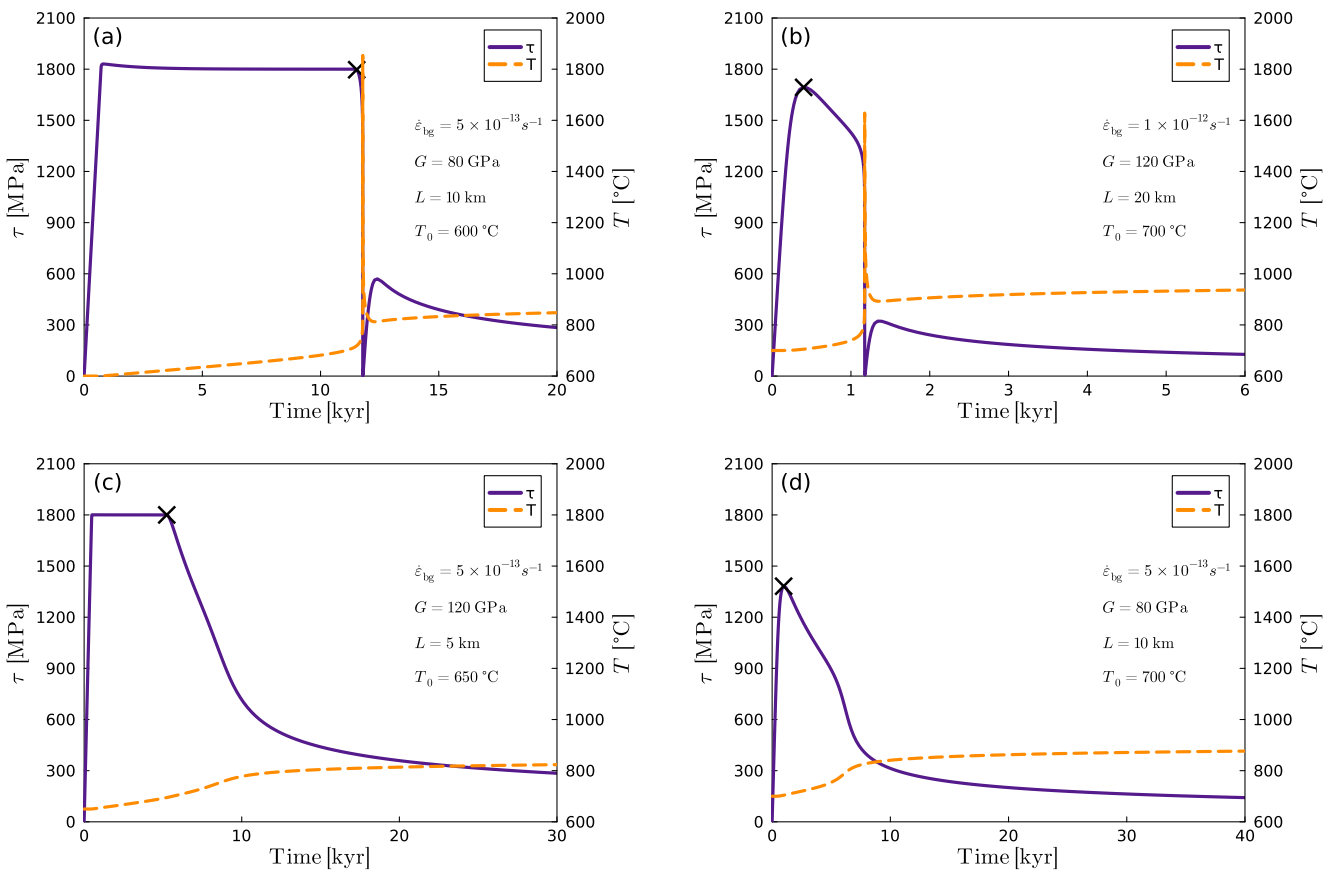

Figure 2. Stress and maximum temperature evolution for representative cases. Models in the left column reached σ_{LTP}, models in the right column did not. (a, b) Thermal runaway occurs, stresses are relaxed quickly with a large temperature surge. (c, d) No thermal runaway occurs, stresses are relaxed with a moderate temperature rise. $\sigma_b = 1.8$ GPa, $\lambda = 3$ J s^{-1} m^{-1} K^{-1}, $\omega_0 = 2$, $h/L = 0.02$ and $\eta_{reg} = 10^{15}$ Pa s for all displayed models.

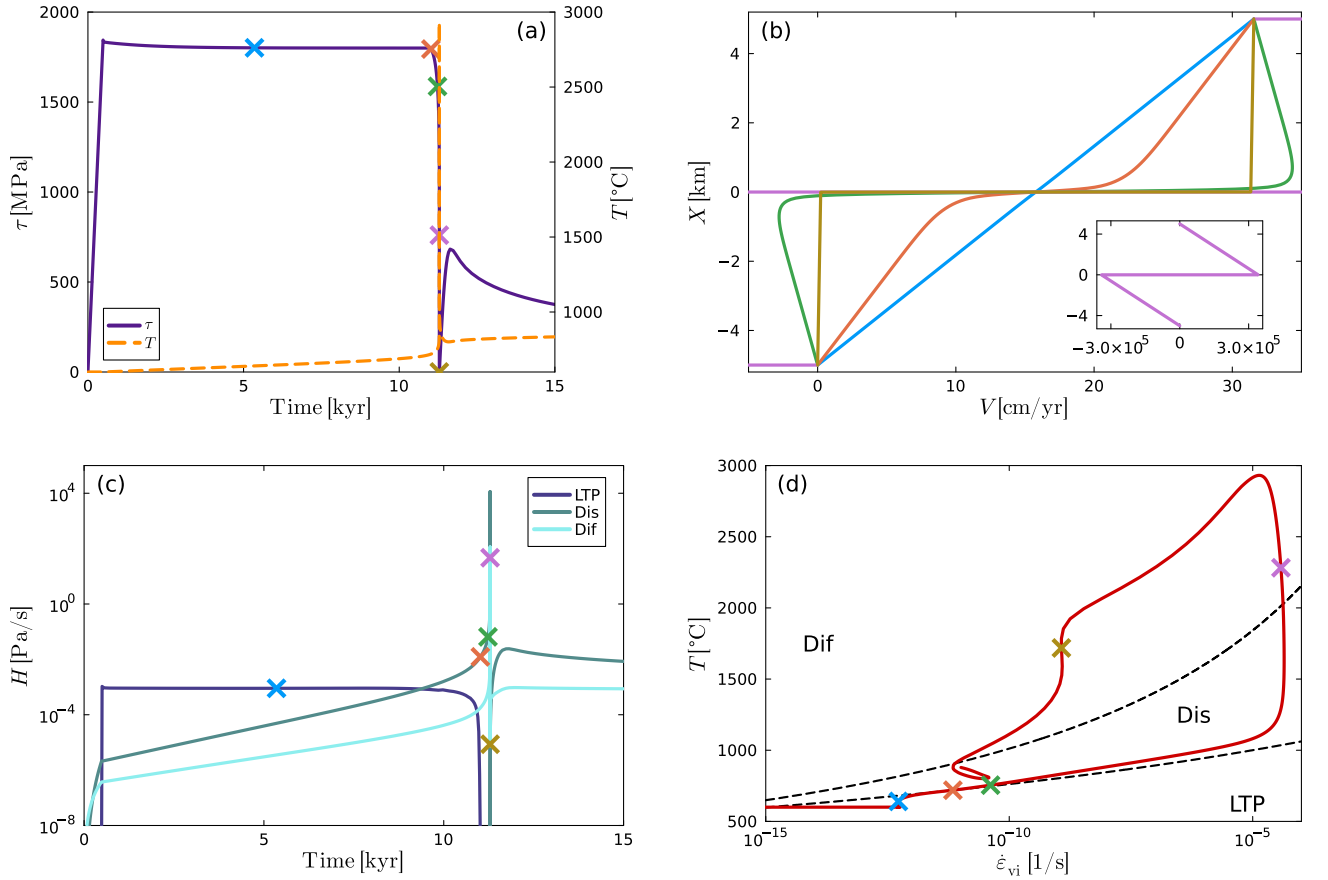

Figure 3. Representative model with thermal runaway. (a) Stress and maximum temperature evolution. Crosses denote time steps that are represented by lines in panel (b) and crosses in panels (c, d). (b) Velocity profile during different stages of the model. Inset shows full range of the purple profile. Colors correspond to the time steps marked by crosses in panel (a). (c) Dissipation of the three viscous deformation mechanisms. (d) Maximum temperature and maximum viscous strain rate evolution on deformation mechanism map from Figure 1b. Note that there are 5 kyr between blue and orange, but only a few seconds between purple and dark yellow. Parameters for this model: $\dot{\varepsilon}_{bg} = 5 \times 10^{-13} s^{-1}$, $G = 120$ GPa, $\sigma_b = 1.8$ GPa, $L = 10$ km, $\lambda = 3$ J s^{-1} m^{-1} K^{-1}, $T_0 = 600$ °C, $\omega_0 = 2$, $h/L = 0.02$, $\eta_{reg} = 10^{13}$ Pa s.

due to shear heating until stresses relax (black crosses in Figure 2) which is accompanied by a steeper temperature increase. At larger initial temperatures, relaxation starts before σ_{LTP} is reached (Figures 2b and 2d).

In all cases, we observe two types of behavior once stress relaxation starts. (a) Stress is relaxed over tens of thousands of years, accompanied by a temperature rise of 100–300 K (Figures 2c and 2d). (b) Stress is relaxed within seconds, accompanied by a temperature surge of up to thousands of Kelvin and a large slip event in the central anomaly (i.e., thermal runaway occurs, Figures 2a and 2b). Runaway may be preceded by a phase of slow relaxation (Figure 2b) or occur immediately after relaxation starts (Figure 2a).

In Figure 3, we show the evolution of stress and maximum temperature (3a), velocity (3b), viscous dissipation (3c), and location on the deformation mechanism map (3d) in a runaway case. While stress is at the LTP-limit, heating occurs mainly due to LTP and the velocity profile is linear. Once dislocation creep takes over inside the anomaly (orange cross in Figure 3), deformation starts to localize in the center and stress decreases. Afterward, the model enters thermal runaway. During this phase, viscous dissipation of diffusion and dislocation creep increase by about six orders of magnitude, accompanied by a slip event in the center (inset in Figure 3b). During the peak of the runaway, diffusion creep shortly becomes the dominant mechanism. As heat subsequently diffuses from the slip zone into the host rock, stress increases again and the model enters a stable sliding regime governed by dislocation creep. In Figure 3d, we illustrate that the transition from LTP to dislocation creep is followed by strong localization (indicated by a strong increase of viscous strain rate in the anomaly) which then causes a temperature surge.

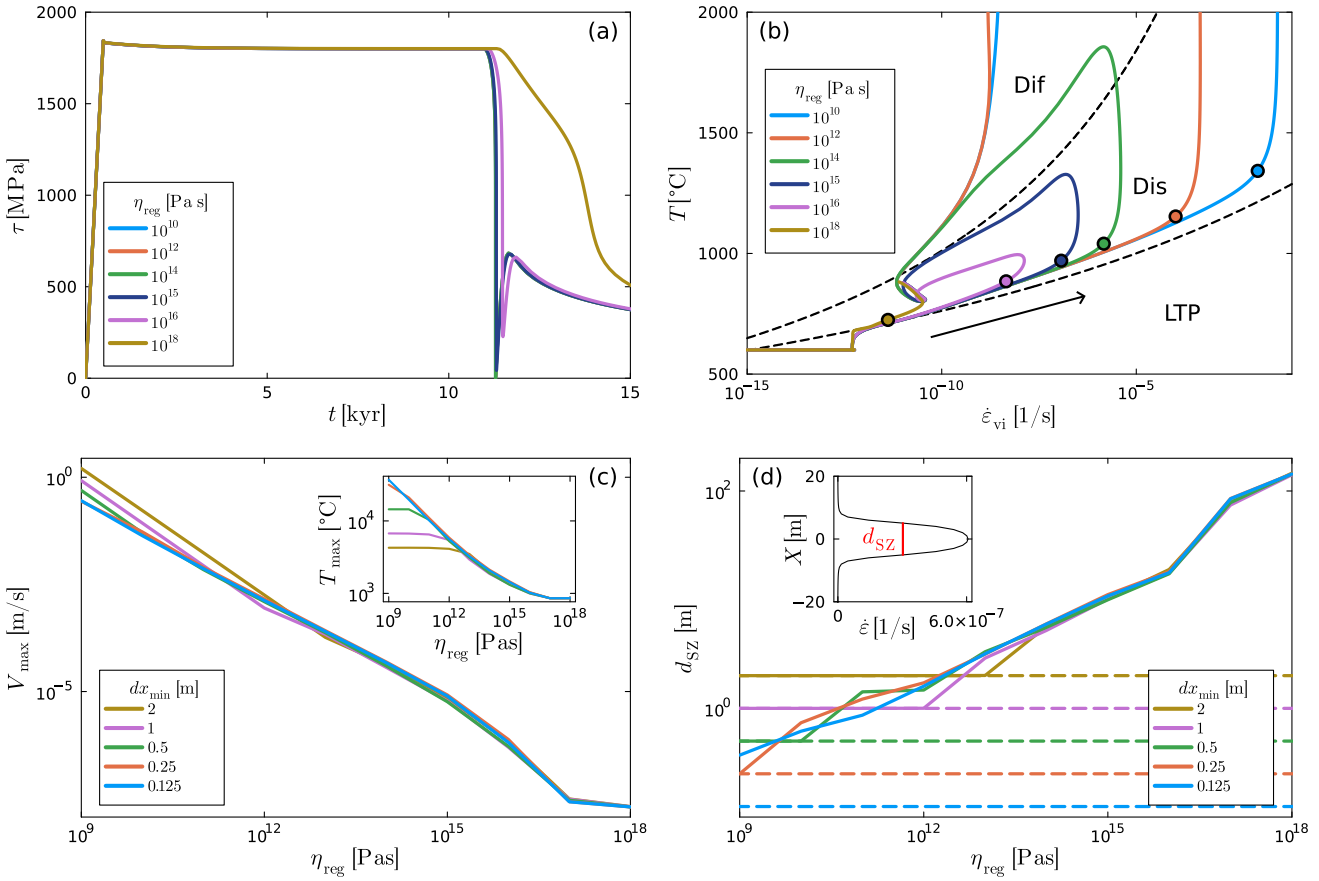

Figure 4. Effects of spatial resolution ($dx_{\min}$) and regularization viscosity (η_{reg}). (a) Temporal evolution of stress for different η_{reg}. Note that simulations with $\eta_{\mathrm{reg}} = 10^{10}$–$10^{15}$ Pa s all plot on top of another. (b) Temperature and viscous strain rate evolution in the center of the model for different η_{reg}. Black dashed lines and labels show the stability fields of the different deformation mechanisms (see Figure 1). Circles indicate when the respective experiments start to be affected by the regularization. Arrow indicates direction of temporal evolution. (c) Maximum slip velocity as function of resolution and η_{reg}. Inset shows maximum temperature. (d) Shear zone thickness (FWHM of strain rate anomaly, see inset) as function of resolution and η_{reg}. Dashed lines indicate the respective size of $dx_{\min}$.

3.2. Regularization

To investigate the effect of the viscosity regularization, we performed 50 simulations with identical parameters ($\dot{\varepsilon}_{\mathrm{bg}} = 5 \times 10^{-13} s^{-1}$, $G = 120$ GPa, $\sigma_{\mathrm{b}} = 1.8$ GPa, $L = 10$ km, $\lambda = 3$ J s^{-1} m^{-1} K^{-1}, $T_0 = 600$ °C, $\omega_0 = 2$, $h/L = 0.02$) but different spatial resolutions $dx_{\min}$ (minimum cell size: 0.125–2 m for a 10 km domain) and regularization viscosities η_{reg} (10^9–10^{18} Pa s). All simulations with $\eta_{\mathrm{reg}} < 10^{15}$ Pa s exhibit the same stress evolution. For larger η_{reg}, localization is restricted by the regularization, resulting in a slower and incomplete stress release (Figure 4a).

In Figure 4b, we show $\dot{\varepsilon}_{\mathrm{vi}}$-$T$-paths of experiments with different regularization viscosities. All models start in LTP, transition to dislocation creep and undergo an increase in viscous strain rate (localization). For models with $\eta_{\mathrm{reg}} < 10^{18}$ Pa s, this is followed by heating (thermal runaway). Independently of η_{reg}, all simulations return to the same location in T-$\dot{\varepsilon}_{\mathrm{vi}}$-space after the runaway due to thermal diffusion. Colored dots indicate when each model starts to be affected by the regularization which prevents the effective viscosity to decrease and strain rate to increase further.

Maximum slip velocities ($V_{\max}$) are inversely correlated with η_{reg} and only become weakly resolution dependent at low η_{reg} (Figure 4c). We observe a similar inverse correlation between η_{reg} and the maximum temperature ($T_{\max}$) which does however break at low η_{reg} (inset of Figure 4c).

To quantify the width of the shear zone (d_{SZ}), we calculate the full-width-half-maximum (FWHM) of the strain rate peak when the model reaches its maximum velocity (see inset in Figure 4d). d_{SZ} decreases exponentially with decreasing η_{reg} and is independent of the spatial resolution until it reaches the size of a single cell (Figure 4d). For example, at $\eta_{reg} = 10^{12}$ Pa s, models with a cell size of 0.5 m or less still show the same shear zone width whereas 1 and 2 m resolution start to deviate.

To summarize, regularization does not impact the evolution of stress or occurrence of thermal runaway for $\eta_{reg} < 10^{15}$ Pa s. It does, however, introduce an upper limit for maximum temperature, slip velocity and strain rate as well as a lower limit for the width of the shear zone. As long as this width is larger than the local resolution, the aforementioned quantities are mesh-independent. Computation time decreases with increasing η_{reg}.

As the parameter study focuses on the occurrence of thermal runaway, we choose $\eta_{reg} = 10^{12}$ Pa s which is low enough to never inhibit it. The central quarter of the cells is a ten-thousandth of the domain size (e.g., 1 m for 10 km, equivalent to purple lines in Figures 4c and 4d). This means that the peak conditions (velocity, temperature etc.) may be resolution dependent and/or limited by regularization, but they are not of interest for the parameter study.

3.3. Nondimensionalization

Thermal runaway occurs for a range of different material parameters and boundary conditions. We find some general trends like high background strain rate and a large model domain leading to thermal runaway more frequently (Figure S1 in Supporting Information S1), but no single parameter can yield a reliable prediction whether runaway occurs or not. To uncover the underlying mechanisms and identify the crucial scales that govern the occurrence of thermal runaway, we nondimensionalize the energy conservation (Equation 5). We define characteristic values for temperature (T_c), stress (τ_c), time (t_c) and length (l_c). Then, each dimensional quantity is replaced by the product of the appropriate characteristic value and the nondimensional quantity:

$$T = T_c\, T', x = l_c\, x', t = t_c\, t', \tau = \tau_c\, \tau', \tag{21}$$

where the subscript $_c$ denotes each characteristic scale and $'$ denotes the nondimensionalized quantities. Applying this scaling to Equation 5 yields:

$$\frac{dT'}{dt'} = t_c \frac{\kappa}{l_c^2} \frac{\partial^2 T'}{\partial x'^2} + \frac{t_c}{T_c} \frac{1}{\rho\, C_p} \tau_c \tau' \dot{\varepsilon}_{vi}, \tag{22}$$

where

$$\kappa = \frac{\lambda}{\rho\, C_p}. \tag{23}$$

Based on the observations in Section 3.1, we make the following assumptions to define the characteristic scales for time, temperature, stress and length:

1. The occurrence of thermal runaway is governed by the conditions when stress relaxation starts (black crosses in Figure 2).
2. Stress relaxation starts after the transition from elastic loading to dislocation creep or after the transition from low-temperature plasticity to dislocation creep.
3. There is no significant amount of temperature change during elastic loading.
4. Temperature change before stress relaxation is homogeneous in the model domain.

Following from these assumptions, we define the characteristic scales as follows:

$$l_c = h, \tag{24}$$

$$T_c = \max(T_0, T_t), \tag{25}$$

$$\tau_c = \min(\tau_{dis,0}, \sigma_b), \tag{26}$$

$$t_c = \frac{\tau_c\ \omega_0}{2\ \dot{\varepsilon}_{bg}\ G}, \tag{27}$$

where

$$T_t = \frac{Q_{dis}}{\ln\left(\frac{\sigma_b^n\ f_{an}\ \omega_0\ A_{dis}}{\dot{\varepsilon}_{bg}}\right)},$$

$$\tau_{dis,0} = \left(\frac{\dot{\varepsilon}_{bg}}{f_{an}\ \omega_0\ A_{dis}} e^{\frac{Q_{dis}}{T_0}}\right)^{\frac{1}{n}}, \tag{28}$$

$$Q_{dis} = \frac{E_{dis}}{R},$$

$$f_{an} = \frac{1}{\omega_0} + \frac{h}{2L}\sqrt{\frac{\pi}{\ln(2)}}\ \frac{\omega_0 - 1}{\omega_0}\mathrm{erf}\left(\frac{L}{h}\sqrt{\ln(2)}\right).$$

h is the full-width-half-maximum of the anomaly, T_0 the initial temperature, σ_b the backstress of LTP, ω_0 the perturbation in the center of the anomaly, $\dot{\varepsilon}_{bg}$ the background strain rate imposed by the boundary conditions, G the shear modulus and f_{an} describes the shape, size and strength of the anomaly. A detailed derivation is presented in Text S2 in Supporting Information S1. Equations 25 and 26 unite the scenarios that reach σ_{LTP} ($T_c = T_t$, $\tau_c = \sigma_b$, Figures 2a and 2c) with those that do not ($T_c = T_0$, $\tau_c = \tau_{dis,0}$, Figures 2b and 2d).

Substituting the characteristic scales l_c and t_c into Equation 22 yields

$$\frac{dT'}{dt'} = \underbrace{\frac{\tau_c\ \omega_0}{2\ \dot{\varepsilon}_{bg}\ G}}_{t_r}\ \underbrace{\frac{\kappa}{h^2}}_{t_d^{-1}}\ \frac{\partial^2 T'}{\partial x'^2} + \underbrace{\frac{1}{\rho\ C_p\ T_c}}_{u_{th}^{-1}}\ \underbrace{\frac{\tau_c^2}{2\ G f_{an}}}_{u_{el}}\ \omega(x)\ \tau'^{n+1}\ e^{\frac{Q_{dis}}{T_c}\frac{T'-1}{T'}}. \tag{29}$$

where t_r is the stress relaxation time scale of the host rock, t_d is the thermal diffusion time scale of the anomaly, u_{th} the thermal energy density and u_{el} the stored elastic energy density (full derivation in Text S2 in Supporting Information S1). For readability, we do not substitute in T_c and τ_c at this point.

3.4. Nondimensional Regimes

The nondimensional analysis suggests that temperature evolution is characterized by two scales. (a) t_r/t_d, the ratio between the characteristic stress relaxation time and the characteristic heat diffusion time. (b) u_{el}/u_{th}, the ratio between the characteristic elastic energy density and the characteristic thermal energy density. This scale represents the conversion of elastic energy to thermal energy during the runaway (e.g., Kameyama et al., 1999; Ogawa, 1987; Regenauer-Lieb & Yuen, 2003). We observe that the entire model domain releases stress (i.e., elastic energy), but the majority of heating occurs in the anomaly. Therefore, we multiply u_{el} by the domain size L and u_{th} by the anomaly size h to obtain absolute energies instead of energy densities. This yields the following 4 scales:

$$t_r = \frac{\tau_c\ \omega_0}{2\ \dot{\varepsilon}_{bg}\ G},$$

$$t_d = \frac{h^2}{\kappa},$$

$$U_{el} = u_{el}\ L = \frac{\tau_c^2\ L}{2\ G\ f_{an}}, \tag{30}$$

$$U_{th} = u_{th}\ h = \rho\ C_p\ T_c\ h.$$

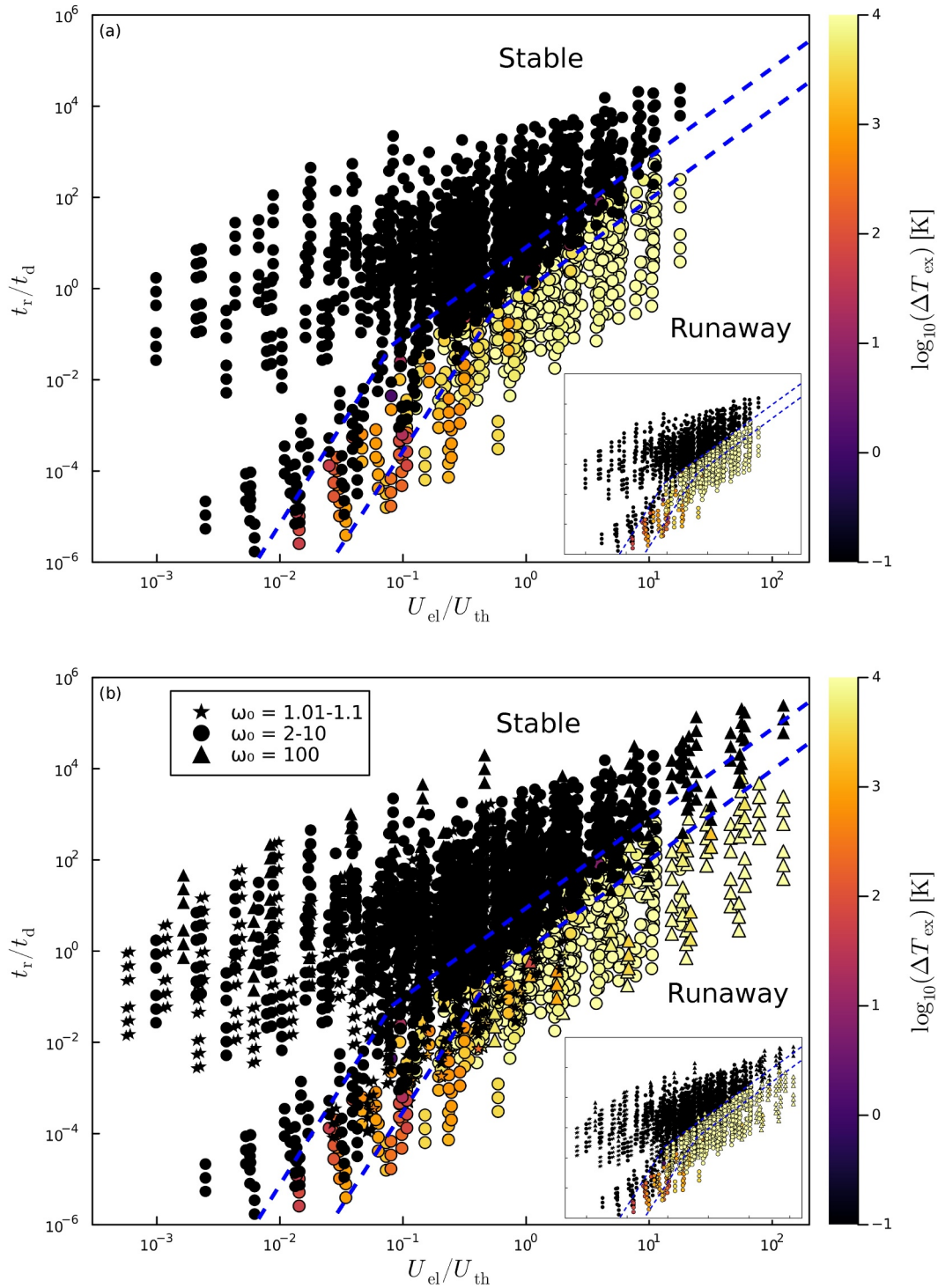

Figure 5. Maximum excess temperature rise ΔT_{ex} as a function of two non-dimensional parameters. t_r/t_d denotes the relation between the stress relaxation time scale and the heat diffusion time scale. U_{el}/U_{th} denotes the ratio between elastic and thermal energy at the start of stress relaxation. Area between dashed blue lines is the transition from the stable to the runaway regime. (a) Models with $\omega_0 = 2 - 10$. (b) All models. Insets show same plots but high ΔT_{ex} plot on top of low ΔT_{ex}. Note that the colorbar is truncated toward low values.

The occurrence of thermal runaway is accompanied by a spike in temperature and velocity, along with a rapid decrease in stress (Figure 3). To identify models with a temperature spike, we calculate ΔT_{ex}, the difference between the maximum temperature and the temperature at the end of the simulation. Plotting ΔT_{ex} against the ratios t_r/t_d and U_{el}/U_{th} reveals that all simulations with an ω_0 between 2 and 10 fall into two regimes with little overlap (Figure 5a). Maximum temperature rise, maximum temperature gradient, maximum stress gradient and maximum velocity increase all show near identical patterns (Figure S2 in Supporting Information S1).

If stress relaxation is fast compared to heat diffusion (low t_r/t_d) and the stored elastic energy is large compared to the thermal energy (high U_{el}/U_{th}), thermal runaway occurs. The regime boundary is well defined for $U_{el}/U_{th} > 0.5$, but changes slope for lower values. Runaway cases at $U_{el}/U_{th} < 0.5$ exhibit lower ΔT_{ex} (i.e., less pronounced temperature peaks).

For $\omega_0 <= 1.1$ and $\omega_0 = 100$, we observe about 50 models that plot in the runaway field without showing the characteristics of thermal runaway (Figure 5b). The causes for these deviations are discussed in Section 4.3.1.

4. Discussion

4.1. Regularization

The regularization introduces a minimum viscosity and consequently limits strain localization, maximum strain rate, maximum velocity and maximum temperature. This facilitates numerical stability and results in shorter solution times. Given the regularization's effects, our velocities and strain rates could be interpreted as lower limit estimates, especially considering that we reach temperatures that should cause melting.

Furthermore, η_{reg} allows us to introduce a grid-independent length scale that controls the minimum width of the localized shear zone. As long as this length scale is larger than the model resolution, shear zone width, maximum slip velocity and maximum temperature are all resolution-independent, showing exponential relationships with η_{reg} (Figure 4).

Up to and including $\eta_{reg} = 10^{15}$ Pa s, we observe no significant changes in the stress evolution of the models (Figure 4a). While this value is large in the context of our study, it is still well below the lower viscosity cut-off of geodynamic models which is commonly 10^{18} Pa s or even higher (e.g., Glerum et al., 2018; Piccolo et al., 2019; Thielmann & Kaus, 2012). This implies that thermal runaway with temperature and velocity spikes, as described in Section 3.1, is unlikely to be observable in large scale geodynamic models. Maximum temperature changes and heating rates in such studies are usually limited (e.g., Devès et al., 2014; Hartz & Podladchikov, 2008; Leloup et al., 1999; Schmalholz & Duretz, 2015; Thielmann & Kaus, 2012).

Goudarzi et al. (2023) discusses a viscosity regularization in the context of brittle earthquakes and reports that η_{reg} is either too high to allow seismic slip velocities or too low to inhibit localization to one grid cell (≈ 2.5 m). We show that ductile deformation at seismic slip rates can indeed be resolved with sub-meter grid cells. In 2D and 3D models, strong grid refinement or alternative solutions such as the phase-field approach, presented in Goudarzi et al. (2023), would be necessary.

4.2. Low-Temperature Plasticity

Diffusion and dislocation creep flow laws for olivine predict viscosities greater than 10^{24} Pa s for the cores of subducting slabs (e.g., Billen, 2010; Karato et al., 2001; Z.-H. Li et al., 2019). Even for strain rates as low as 10^{-15} s^{-1}, these viscosities imply stresses of more than 2 GPa. As LTP limits stresses to less than 2 GPa, it plays a crucial role in such settings. Under loading, LTP causes stress to plateau for several thousand years before temperatures are high enough for dislocation creep to relax the stress and potentially trigger thermal runaway.

This has implications for studies that do not include LTP in their rheological model. Unless initial temperatures are high enough for other creep mechanisms to limit stresses to less than 2 GPa, the models will reach conditions that should be naturally inadmissible as demonstrated by Kameyama et al. (1999). This leads to much more violent runaway events as the released elastic energy is proportional to the square of the stress before release (Equation 29). As an example, the parameter set used for Figure 4 with $\eta_{reg} = 10^{12}$ Pa s produces a maximum temperature of 144′000 °C when LTP is not considered compared to 5′500 °C with LTP.

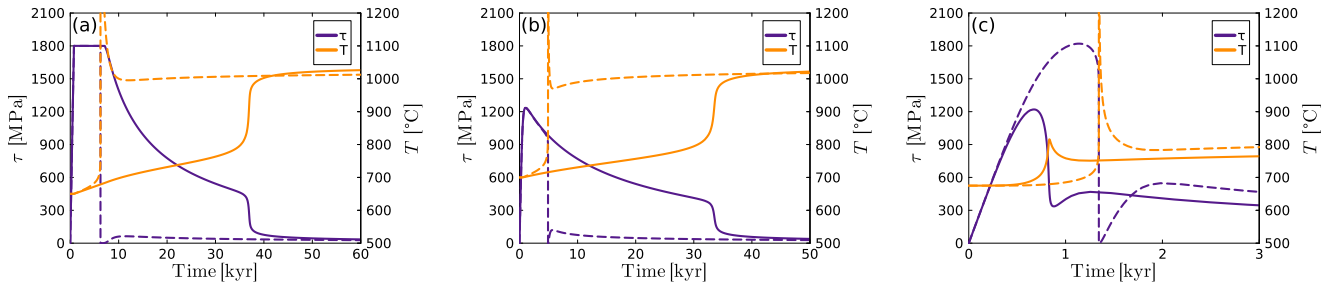

Figure 6. Failed runaways. Solid lines show stress (purple) and temperature evolution (orange) for representative models that did not experience thermal runaway but plot inside the runaway regime (Figure 5b). (a, b) $\omega_0 <= 1.1$ with delayed stress localization. Dashed lines show the same parameter combinations with $\omega_0 = 2$ exhibiting thermal runaway. (c) $\omega_0 = 100$ with incomplete localization. Dashed lines show the same model with $\omega_0 = 10$ exhibiting thermal runaway.

The influence of LTP also complicates the definition of a critical stress that can trigger thermal runaway as presented by Braeck et al. (2009) because this critical stress might be unreachable due to LTP. Instead, LTP allows for models to significantly heat up at the LTP-limit and eventually enter thermal runaway at much lower stresses than would be predicted by a scaling law not considering LTP. Whether LTP helps or hinders thermal runaway is discussed in Section 4.3.2.

There is still little consensus on the correct flow law and parameters for LTP in geodynamic models (Jain et al., 2017; Kumamoto et al., 2017). For the temperature window of this study, different flow laws yield peak stresses between 1 and 3 GPa (Gouriet et al., 2019; Toffol et al., 2022). Given, the weak temperature dependence of Equation 16, σ_b provides good control over σ_{LTP} and we varied it between 0.9 and 2.7 GPa to cover this range. The pressure dependence of LTP is also controversial as Jain et al. (2017) constrain it to be close to zero while Kawazoe et al. (2009) conclude a significant strengthening with depth, reaching almost 4 GPa at 300 km depth. Kumamoto et al. (2017) attribute most of this discrepancy to differences in sample grain size and indentation technique. Generally, a high LTP limit favors thermal runaway as discussed in Section 4.3.2.

4.3. Nondimensional Scales

Elastic loading, heating at the LTP-limit, stress relaxation, thermal runaway, reloading and repeated relaxation are all transient processes that depend on the current conditions, opposed to the initial conditions and are therefore inherently difficult to predict. This problem gets amplified by nonlinear relationships such as composite rheologies that include dislocation creep and/or LTP. On top of that, heat diffusion causes time- and space-dependent temperature conditions while strain localization does the same to strain rate conditions and reduces the size of the anomaly.

To approach this challenge, we decide to approximate the conditions at stress release by the transition from elastic or LTP-dominated to dislocation creep-dominated deformation (Equations 25–27). Furthermore, we assume that beyond these conditions, the system is entirely governed by dislocation creep and disregard diffusion creep. This allows us to identify two nondimensional numbers (t_r/t_d and U_{el}/U_{th}) that can estimate the occurrence of thermal runaway based on the material's rheological and thermal properties, size of system and anomaly, as well as initial temperature and background strain rate.

t_r/t_d describes the competition between heating by stress relaxation and cooling by diffusion, a concept already described by Gruntfest (1963) that reappears in different studies on ductile localization (e.g., Kiss et al., 2019; Ogawa, 1987; Yuen et al., 1978). U_{el}/U_{th} is the ratio of elastic to thermal energy at stress release. The conversion of the former into the latter has been named as the driver of thermal runaway (e.g., Kameyama et al., 1999; Ogawa, 1987; Regenauer-Lieb & Yuen, 2003). Thermal runaway is facilitated by a low t_r/t_d (i.e., stress release is faster than thermal diffusion) and a high U_{el}/U_{th} (i.e., stress and deforming domain are large while temperature is low).

Despite the aforementioned transient processes and nonlinear relationships, these two ratios split all experiments with $2.0 <= \omega_0 <= 10$ into a stable and runaway regime (Figure 5a). The regime boundary follows the relationship $t_r/t_d \propto (U_{el}/U_{th})^2$ for most models, but bends toward a minimum U_{el}/U_{th} of about 10^{-3}. This suggests that there is a minimum required energy ratio to cause thermal runaway. Braeck et al. (2009) observe a similarly

shaped regime boundary for the initial stress which they term "critical stress." In Text S1 in Supporting Information S1, we present an extension of the scaling relationship that also accounts for diffusion creep. This extension has no effect on the 6,000 models plotted in Figure 5.

4.3.1. Failed Runaway

Figure 5b shows that about 5% of models with $\omega_0 <= 1.1$ or $\omega_0 = 100$ do not undergo thermal runaway despite falling in the runaway regime. The vast majority of these models have an $\omega_0 <= 1.1$ and share a common feature: As the difference between host rock and anomaly is very small, localization is slower than stress relaxation. This means that large portions of the stored elastic energy are converted to heat outside the anomaly, thus violating the assumptions that the scaling is based on. When these models localize, there is not enough elastic energy left to cause a temperature spike. Many of them still show a period of rapid stress drop and temperature rise toward the end of the relaxation (solid lines in Figures 6a and 6b), but they are much closer to what Braeck et al. (2009) termed "adiabatic runaway." If the scaling could account for the delayed, and therefore smaller, stress drop, these models would plot at lower U_{el}/U_{th} in the stable regime (Figure 5b).

For the few models with $\omega_0 = 100$ that do not undergo runaway despite falling in the runaway regime, we propose that the difference between host rock and anomaly is too large for the models to exhibit progressive localization inside the anomaly. Consequently, heat is distributed in a larger area and the anomaly does not weaken enough to result in thermal runaway. Five out of seven of these models result in thermal runaway for lower values of ω_0 (dashed lines in Figure 6c). The fact that some settings are more likely to result in thermal runaway by increasing ω_0 (Figures 6a and 6b) and others by decreasing ω_0 (Figure 6c) demonstrates the complex transient interactions that are difficult to fully capture in a scaling.

4.3.2. Comparison to Previous Studies

In this study, we propose that thermal runaway is governed by the ratios t_r/t_d and U_{el}/U_{th}. Similar nondimensional scalings have been proposed in previous studies. Ogawa (1987) presents three scales, the Gruntfest number (Gruntfest, 1963), similar to the inverse of t_r/t_d, a ratio of elastic to ductile stiffness which bears similarities with the inverse of U_{el}/U_{th} and a quantity characterizing the anomaly strength and size. Braeck et al. (2009) include the anomaly description into the other two scales to reduce the problem to two ratios. The first of which is almost identical to t_r/t_d whereas the second one relates the boundary stress to a critical stress derived from an analytical solution. Furthermore, our characterization of the anomaly $\left(f_{an}\right)$ is similar to the one used by Braeck et al. (2009). Both of the previous studies describe a rheology consisting of elasticity and dislocation creep, neglecting the stress-limiting effect of LTP which is included in Equation 29 and the potential interference of diffusion creep. On top of that, the study of Braeck et al. (2009) applies stress boundary conditions which exclude the transient effects that occur during loading and LTP.

The nondimensional scaling also agrees with previous studies which show that higher background strain rates (lower t_r/t_d) facilitate thermal runaway while higher initial temperatures (larger U_{el}/U_{th}) hamper it (Kameyama et al., 1999; Kaus & Podladchikov, 2006; Thielmann, 2018).

Kameyama et al. (1999) concluded that LTP inhibits thermal runaway for constant strain rate boundary conditions by lowering the maximum stress and thereby the amount of viscous dissipation. Given the quadratic dependence of U_{el}/U_{th} on maximum shear stress (Equation 30), LTP does in fact have a negative effect on thermal runaway probability at low temperatures. It does, however, not inhibit it (Figures 2–4), and often just delays the runaway. The reason LTP inhibited runaway in Kameyama et al. (1999) is the use of a thermal anomaly which diffuses away during the delay caused by LTP. Kelemen and Hirth (2007) also argue that LTP inhibits runaway at high stresses by distributing deformation over a large area, but our models demonstrate that, eventually, the anomaly will transition to dislocation and initialize thermal runaway.

4.4. Design Choices and Limitations

Numerical models inherently involve some artificial components like the initial anomaly (Figure 1a). The majority of previous studies chose a temperature perturbation (Braeck et al., 2009; Kameyama et al., 1999; Kaus & Podladchikov, 2006; Kiss et al., 2019; Ogawa, 1987; Yuen et al., 1978) whereas we use a rheological perturbation, similar to Thielmann et al. (2015). Such a local change in material property is consistent with a

heterogeneity in composition or water content and has the advantage of being independent of time (John et al., 2009). Thermal anomalies diffuse over time and smear out for low strain rates (e.g., Kameyama et al., 1999) and small anomalies (e.g., Ogawa, 1987).

Another arbitrary choice is the shape of the perturbation. The majority of previous studies used a step-like perturbation with a sharp boundary and constant value wheres Yuen et al. (1978) employed a Gaussian-like perturbation. We tested both and observed that the Gaussian perturbation facilitates localization for large anomalies. In 131 cases, a step-like anomaly did not result in runaway whereas a Gaussian anomaly did (Figure S3 in Supporting Information S1). There is also a very small number of cases (less than 10 out of 6,000), where the step-like anomaly resulted in runaway and the Gaussian perturbation did not.

Our rheological model does not account for the possibility of brittle failure and the ultimate strength of the crystal lattice. The Drucker-Prager yield criterion (Drucker & Prager, 1952) predicts a yield strength of 5 GPa for a pressure of 10 GPa (Table 1) and a typical friction angle of 30°. The theoretical strength of atomic bonds is on the order 10% of the shear modulus (Renshaw & Schulson, 2007) which equates to 4–16 GPa for our parameter range. With LTP, such stresses are unreachable.

We neglect the inertial terms from Equation 4 and do not account for melting. Both of these simplifications have no impact on the occurrence of thermal runaway. During the later stages of the runaway, emission of seismic waves and melting would, however, act as energy sinks and limit the peak temperatures. Adding more spatial dimensions would allow for cooling of the shear zone by injection veins (e.g., Andersen et al., 2014) and limitation of slip rates by a finite fault length.

Adding grain size evolution to our rheological model or using a smaller initial grain size would likely result in lower characteristic stresses. Given the quadratic dependence of U_{el}/U_{th} compared to the linear dependence of t_r/t_d on τ_c, this would reduce the likelihood of thermal runaway. Thielmann (2018) shows a similar result where a reduced initial grain size shifts the regime boundary toward lower temperatures, similarly, Foley (2018) concludes that grain size evolution limits the effect of shear heating. However, Cross and Skemer (2019) suggest that dynamic recrystallization (i.e., grain size reduction) is strain dependent and that only about 10% of olivine grains recrystallize at a strain of 1 for olivine. Since our models all release their stress before reaching a strain of 1 (many at less than 0.1), we would not expect a significant amount of grain size reduction that could influence the thermal runaway.

4.5. Implications for Deep Earthquakes

Our models demonstrate that thermal runaway can occur within the cores of subducting slabs, at all tested strain rates (10^{-14} s^{-1} to 5×10^{-12} s^{-1}). This is significantly lower than the window of 10^{-11} s^{-1} to 10^{-9} s^{-1} suggested by Gasc et al. (2022). During the runaway, maximum slip velocities and strain rates reach the values associated with pseudotachylyte formation ($v \approx 1$ m s^{-1}, $\dot{\varepsilon} \approx 1$ s^{-1}; Del Gaudio et al., 2009; Spray, 1995) which are commonly interpreted as the products of deep earthquakes (e.g., Andersen et al., 2008; Deseta et al., 2014). With a regularization viscosity of 10^{15} Pa s, our models predict a temperature increase of about 1000 K (Figures 2a and 2b). This is in line with estimates of 600–1000 K for intermediate-depth earthquakes of the Bucaramanga Nest which are based on stress drop and slip (Prieto et al., 2013).

In our simulations, runaway occurred at as low as 400 MPa deviatoric stress, but the majority of models reached between 1 and 2 GPa. As discussed in Section 4.2, olivine flow laws imply such stresses for the interior of subducting slabs at strain rates $>10^{-15}$ s^{-1}. For lower strain rates, additional processes may also locally increase stresses. Dehydration-driven stress transfer (for intermediate-depth earthquakes, Ferrand et al., 2017) and the volume change due to the olivine-spinel-transformation (for deep-focus earthquakes, Liu et al., 1998) are reaction-based stress sources. Furthermore, geodynamic models by Toffol et al. (2022) suggest that stress amplifications around weak inclusions can be on the order of a few GPa. Lastly, the resistance of the 660 km discontinuity causes compressional stresses along the slab (Zhan, 2020) which can result in folding. The consequences of a folded slab are large zones of amplified stress and strain.

Like in previous work (e.g., Braeck et al., 2009; Kelemen & Hirth, 2007; Thielmann et al., 2015), thermal runaway results in a complete release of stress in our study while models of brittle earthquakes usually show partial stress release (e.g., Dal Zilio et al., 2022; M. Li et al., 2022). This is in line with observations of larger stress drops in deep earthquakes compared to shallow ones (Frohlich, 1989). The large stress drops are a consequence of the self-feeding nature of thermal runaway that continuously weakens the shear zone.

We observe thermal runaway with rheological perturbations as low as 1% ($\omega_0 = 1.01$) which suggests that natural heterogeneities in composition, water content, or anisotropy could all be sufficient triggers for deep earthquakes. The quadratic, inverse dependence of t_r/t_d on the perturbation size h does however indicate that thermal runaway is unlikely to initiate at the mm-scale. Thermal runaway could therefore be the second phase of a dual-mechanism process which is initiated by a different mechanism (e.g., Bezada & Humphreys, 2012; McGuire et al., 1997; Zhan, 2020). In the case of intermediate-depth earthquakes, a stress perturbation caused by dehydration embrittlement, dehydration-driven stress transfer or a weak inclusion could trigger thermal runaway. For deep-focus earthquakes, transformational faulting could weaken an area of metastable olivine at the grain scale before thermal runaway initiates as a result of this weakening. As deep-focus earthquakes are not limited to the extent of the metastable olivine wedge, thermal runaway could be the mechanism which allows them to propagate into the warmer areas of the slab (Zhan, 2017).

In many of our simulations, LTP delays thermal runaway by about 10 kyr. Assuming a sinking velocity of 10 cm/yr, this would only displace the slab by 1 km which is insignificant on the scales of a subduction. Furthermore, the delay by LTP is a function of the difference between the starting temperature and the transition temperature where dislocation creep becomes dominant. Thus, one area of the slab should always be in the correct temperature window for a weak seed to initiate thermal runaway without delay. Consequently, the delay observed in some of our models does not rule out the involvement of thermal runaway in multi-stage rupture processes that are sometimes observed for deep earthquakes (Bezada & Humphreys, 2012; Fan et al., 2019; Ye et al., 2016).

5. Conclusions

In this study, we present thermomechanical 1D models of velocity-driven simple-shear deformation with a visco-elastic rheology comprising diffusion creep, dislocation creep and LTP. The rheological model is augmented by a regularization viscosity that provides numerical stability during strain localization and limits resolution dependencies. Low-temperature plasticity plays a critical role in this system, limiting deviatoric stresses and thereby delaying thermal runaway by up to thousands of years.

We observe shear zone formation accompanied by a moderate (100–300 K) temperature increase or thermal runaway accompanied by strong localization and a temperature surge of thousands of Kelvin. We derive two nondimensional ratios that combine initial conditions and material parameters and allow us to estimate the occurrence of thermal runaway. t_r/t_d describes the competition of heat generation from stress relaxation and heat loss due to thermal diffusion whereas U_{el}/U_{th} compares the stored elastic energy to thermal energy in the system. Thermal runaway occurs if t_r/t_d is small and U_{el}/U_{th} is large.

Our numerical experiments demonstrate that thermal runaway is a viable mechanism to cause fast slip events that are in line with intermediate- and deep-focus earthquakes, as well as pseudotachylyte formation at conditions comparable to cores of subducting slabs. The nondimensional scaling indicates that thermal runaway is unlikely to initiate at the grain scale, but can act as the second stage of a dual-mechanism rupture process.

Acknowledgments
We thank Alexandre Schubnel, Pietro Sternai, Giovanni Toffol and Ylona van Dinther for their constructive and encouraging comments. A.S. and M.T. were funded by the DFG Grant TH 2076/8-1 awarded to M.T.. D.K. acknowledges the European Research Council (Consolidator Grant 771143 (MAGMA) awarded to Boris J.P. Kaus), the Research Council of Norway and the industry partners of NCS2030 (RCN project number 331644) for their support. Open Access funding enabled and organized by Projekt DEAL.

Data Availability Statement

Figures were made with Plots.jl, version 1.40.4 (Breloff, 2024), available on zenodo at https://zenodo.org/records/10959005. The code we developed and used for this study (Spang et al., 2024) is available on zenodo at https://doi.org/10.5281/zenodo.12167393.

References

Andersen, T. B., Austrheim, H., Deseta, N., Silkoset, P., & Ashwal, L. D. (2014). Large subduction earthquakes along the fossil Moho in Alpine Corsica. *Geology*, *42*(5), 395–398. https://doi.org/10.1130/g35345.1

Andersen, T. B., Mair, K., Austrheim, H., Podladchikov, Y. Y., & Vrijmoed, J. C. (2008). Stress release in exhumed intermediate and deep earthquakes determined from ultramafic pseudotachylyte. *Geology*, *36*(12), 995–998. https://doi.org/10.1130/g25230a.1

Austin, N., Evans, B., Herwegh, M., & Ebert, A. (2008). Strain localization in the Morcles nappe (Helvetic Alps, Switzerland). *Swiss Journal of Geosciences*, *101*(2), 341–360. https://doi.org/10.1007/s00015-008-1264-2

Barnes, J., Selverstone, J., & Sharp, Z. (2004). Interactions between serpentinite devolatilization, metasomatism and strike-slip strain localization during deep-crustal shearing in the Eastern Alps. *Journal of Metamorphic Geology*, *22*(4), 283–300. https://doi.org/10.1111/j.1525-1314.2004.00514.x

Bercovici, D., & Karato, S.-i. (2002). Theoretical analysis of shear localization in the lithosphere. *Reviews in Mineralogy and Geochemistry*, *51*(1), 387–420. https://doi.org/10.2138/gsrmg.51.1.387

Bercovici, D., & Ricard, Y. (2012). Mechanisms for the generation of plate tectonics by two-phase grain-damage and pinning. *Physics of the Earth and Planetary Interiors*, *202*, 27–55. https://doi.org/10.1016/j.pepi.2012.05.003

Bezada, M., & Humphreys, E. (2012). Contrasting rupture processes during the April 11, 2010 deep-focus earthquake beneath Granada, Spain. *Earth and Planetary Science Letters*, *353*, 38–46. https://doi.org/10.1016/j.epsl.2012.08.001

Billen, M. I. (2010). Slab dynamics in the transition zone. *Physics of the Earth and Planetary Interiors*, *183*(1–2), 296–308. https://doi.org/10.1016/j.pepi.2010.05.005

Braeck, S., & Podladchikov, Y. (2007). Spontaneous thermal runaway as an ultimate failure mechanism of materials. *Physical Review Letters*, *98*(9), 095504. https://doi.org/10.1103/physrevlett.98.095504

Braeck, S., Podladchikov, Y. Y., & Medvedev, S. (2009). Spontaneous dissipation of elastic energy by self-localizing thermal runaway. *Physical Review E*, *80*(4), 046105. https://doi.org/10.1103/physreve.80.046105

Braun, J., Chéry, J., Poliakov, A., Mainprice, D., Vauchez, A., Tomassi, A., & Daignières, M. (1999). A simple parameterization of strain localization in the ductile regime due to grain size reduction: A case study for olivine. *Journal of Geophysical Research*, *104*(B11), 25167–25181. https://doi.org/10.1029/1999jb900214

Breloff, T. (2024). Plots.jl [Software]. *Zenodo*. https://doi.org/10.5281/zenodo.10959005

Brinkman, H. (1951). Heat effects in capillary flow i. *Applied Scientific Research*, *2*(1), 120–124. https://doi.org/10.1007/bf00411976

Burnley, P. C., Green, H. W., & Prior, D. J. (1991). Faulting associated with the olivine to spinel transformation in Mg_2GeO_4 and its implications for deep-focus earthquakes. *Journal of Geophysical Research*, *96*(B1), 425–443. https://doi.org/10.1029/90jb01937

Byerlee, J. (1978). Friction of rocks. In *Rock friction and earthquake prediction* (pp. 615–626). Birkhäuser.

Chrysochoos, A., & Belmahjoub, F. (1992). Thermographic analysis of thermomechanical couplings. *Archives of Mechanics*, *44*(1), 55–68.

Cross, A., & Skemer, P. (2019). Rates of dynamic recrystallization in geologic materials. *Journal of Geophysical Research: Solid Earth*, *124*(2), 1324–1342. https://doi.org/10.1029/2018jb016201

Dal Zilio, L., Lapusta, N., Avouac, J.-P., & Gerya, T. (2022). Subduction earthquake sequences in a non-linear visco-elasto-plastic megathrust. *Geophysical Journal International*, *229*(2), 1098–1121. https://doi.org/10.1093/gji/ggab521

De Borst, R., Sluys, L. J., Muhlhaus, H.-B., & Pamin, J. (1993). Fundamental issues in finite element analyses of localization of deformation. *Engineering Computations*, *10*(2), 99–121. https://doi.org/10.1108/eb023897

Del Gaudio, P., Di Toro, G., Han, R., Hirose, T., Nielsen, S., Shimamoto, T., & Cavallo, A. (2009). Frictional melting of peridotite and seismic slip. *Journal of Geophysical Research*, *114*(B6). https://doi.org/10.1029/2008jb005990

Deseta, N., Andersen, T., & Ashwal, L. (2014). A weakening mechanism for intermediate-depth seismicity? Detailed petrographic and microtextural observations from blueschist facies pseudotachylytes, Cape Corse, Corsica. *Tectonophysics*, *610*, 138–149. https://doi.org/10.1016/j.tecto.2013.11.007

Devès, M. H., Tait, S. R., King, G. C., & Grandin, R. (2014). Strain heating in process zones; implications for metamorphism and partial melting in the lithosphere. *Earth and Planetary Science Letters*, *394*, 216–228. https://doi.org/10.1016/j.epsl.2014.03.002

Drucker, D. C., & Prager, W. (1952). Soil mechanics and plastic analysis or limit design. *Quarterly of Applied Mathematics*, *10*(2), 157–165. https://doi.org/10.1090/qam/48291

Duretz, T., de Borst, R., Yamato, P., & Le Pourhiet, L. (2020). Toward robust and predictive geodynamic modeling: The way forward in frictional plasticity. *Geophysical Research Letters*, *47*(5), e2019GL086027. https://doi.org/10.1029/2019gl086027

Duretz, T., Räss, L., Podladchikov, Y., & Schmalholz, S. (2019). Resolving thermomechanical coupling in two and three dimensions: Spontaneous strain localization owing to shear heating. *Geophysical Journal International*, *216*(1), 365–379. https://doi.org/10.1093/gji/ggy434

Duretz, T., Schmalholz, S., Podladchikov, Y., & Yuen, D. (2014). Physics-controlled thickness of shear zones caused by viscous heating: Implications for crustal shear localization. *Geophysical Research Letters*, *41*(14), 4904–4911. https://doi.org/10.1002/2014gl060438

Fan, W., Wei, S. S., Tian, D., McGuire, J. J., & Wiens, D. A. (2019). Complex and diverse rupture processes of the 2018 M w 8.2 and M w 7.9 Tonga-Fiji deep earthquakes. *Geophysical Research Letters*, *46*(5), 2434–2448. https://doi.org/10.1029/2018gl080997

Ferrand, T. P., Hilairet, N., Incel, S., Deldicque, D., Labrousse, L., Gasc, J., et al. (2017). Dehydration-driven stress transfer triggers intermediate-depth earthquakes. *Nature Communications*, *8*(1), 15247. https://doi.org/10.1038/ncomms15247

Foley, B. J. (2018). On the dynamics of coupled grain size evolution and shear heating in lithospheric shear zones. *Physics of the Earth and Planetary Interiors*, *283*, 7–25. https://doi.org/10.1016/j.pepi.2018.07.008

Frankel, S. P. (1950). Convergence rates of iterative treatments of partial differential equations. *Mathematics of Computation*, *4*(30), 65–75. https://doi.org/10.1090/s0025-5718-1950-0046149-3

Frohlich, C. (1989). The nature of deep-focus earthquakes. *Annual Review of Earth and Planetary Sciences*, *17*(1), 227–254. https://doi.org/10.1146/annurev.ea.17.050189.001303

Gasc, J., Daigre, C., Moarefvand, A., Deldicque, D., Fauconnier, J., Gardonio, B., et al. (2022). Deep-focus earthquakes: From high-temperature experiments to cold slabs. *Geology*, *50*(9), 1018–1022. https://doi.org/10.1130/g50084.1

Gerya, T. V., & Yuen, D. A. (2003). Characteristics-based marker-in-cell method with conservative finite-differences schemes for modeling geological flows with strongly variable transport properties. *Physics of the Earth and Planetary Interiors*, *140*(4), 293–318. https://doi.org/10.1016/j.pepi.2003.09.006

Getsinger, A., Hirth, G., Stünitz, H., & Goergen, E. (2013). Influence of water on rheology and strain localization in the lower continental crust. *Geochemistry, Geophysics, Geosystems*, *14*(7), 2247–2264. https://doi.org/10.1002/ggge.20148

Glerum, A., Thieulot, C., Fraters, M., Blom, C., & Spakman, W. (2018). Nonlinear viscoplasticity in aspect: Benchmarking and applications to subduction. *Solid Earth*, *9*(2), 267–294. https://doi.org/10.5194/se-9-267-2018

Goudarzi, M., Gerya, T., & Dinther, Y. v. (2023). A comparative analysis of continuum plasticity, viscoplasticity and phase-field models for earthquake sequence modeling. *Computational Mechanics*, *72*(4), 615–633. https://doi.org/10.1007/s00466-023-02311-0

Gouriet, K., Cordier, P., Garel, F., Thoraval, C., Demouchy, S., Tommasi, A., & Carrez, P. (2019). Dislocation dynamics modelling of the power-law breakdown in olivine single crystals: Toward a unified creep law for the upper mantle. *Earth and Planetary Science Letters*, *506*, 282–291. https://doi.org/10.1016/j.epsl.2018.10.049

Green, H., & Houston, H. (1995). The mechanics of deep earthquakes. *Annual Review of Earth and Planetary Sciences*, *23*(1), 169–213. https://doi.org/10.1146/annurev.ea.23.050195.001125

Green, H., II, & Burnley, P. (1989). A new self-organizing mechanism for deep-focus earthquakes. *Nature*, *341*(6244), 733–737. https://doi.org/10.1038/341733a0

Gruntfest, I. (1963). Thermal feedback in liquid flow; plane shear at constant stress. *Transactions of the Society of Rheology*, *7*(1), 195–207. https://doi.org/10.1122/1.548954

Hacker, B. R., Peacock, S. M., Abers, G. A., & Holloway, S. D. (2003). Subduction factory 2. Are intermediate-depth earthquakes in subducting slabs linked to metamorphic dehydration reactions? *Journal of Geophysical Research*, *108*(B1). https://doi.org/10.1029/2001jb001129

Hansen, L. N., Kumamoto, K. M., Thom, C. A., Wallis, D., Durham, W. B., Goldsby, D. L., et al. (2019). Low-temperature plasticity in olivine: Grain size, strain hardening, and the strength of the lithosphere. *Journal of Geophysical Research: Solid Earth*, *124*(6), 5427–5449. https://doi.org/10.1029/2018jb016736

Hartz, E. H., & Podladchikov, Y. Y. (2008). Toasting the jelly sandwich: The effect of shear heating on lithospheric geotherms and strength. *Geology*, *36*(4), 331–334. https://doi.org/10.1130/g24424a.1

Hirth, G., & Kohlstedt, D. L. (2003). Rheology of the upper mantle and the mantle wedge: A view from the experimentalists. *Geophysical Monograph-American Geophysical Union*, *138*, 83–106.

Hobbs, B., Ord, A., & Teyssier, C. (1986). Earthquakes in the ductile regime? *Pure and Applied Geophysics*, *124*(1–2), 309–336. https://doi.org/10.1007/bf00875730

Holtzman, B., Chrysochoos, A., & Daridon, L. (2018). A thermomechanical framework for analysis of microstructural evolution: Application to olivine rocks at high temperature. *Journal of Geophysical Research: Solid Earth*, *123*(10), 8474–8507. https://doi.org/10.1029/2018jb015613

Houston, H. (2015). Deep earthquakes. In *Treatise on geophysics*. Elsevier.

Iordache, M.-M., & Willam, K. (1998). Localized failure analysis in elastoplastic Cosserat continua. *Computer Methods in Applied Mechanics and Engineering*, *151*(3–4), 559–586. https://doi.org/10.1016/s0045-7825(97)00166-7

Jacquey, A. B., & Cacace, M. (2020). Multiphysics modeling of a brittle-ductile lithosphere: 1. Explicit visco-elasto-plastic formulation and its numerical implementation. *Journal of Geophysical Research: Solid Earth*, *125*(1), e2019JB018474. https://doi.org/10.1029/2019jb018474

Jacquey, A. B., Rattez, H., & Veveakis, M. (2021). Strain localization regularization and patterns formation in rate-dependent plastic materials with multiphysics coupling. *Journal of the Mechanics and Physics of Solids*, *152*, 104422. https://doi.org/10.1016/j.jmps.2021.104422

Jain, C., Korenaga, J., & Karato, S.-i. (2017). On the yield strength of oceanic lithosphere. *Geophysical Research Letters*, *44*(19), 9716–9722. https://doi.org/10.1002/2017gl075043

Jamtveit, B., Austrheim, H., & Putnis, A. (2016). Disequilibrium metamorphism of stressed lithosphere. *Earth-Science Reviews*, *154*, 1–13. https://doi.org/10.1016/j.earscirev.2015.12.002

John, T., Medvedev, S., Rüpke, L. H., Andersen, T. B., Podladchikov, Y. Y., & Austrheim, H. (2009). Generation of intermediate-depth earthquakes by self-localizing thermal runaway. *Nature Geoscience*, *2*(2), 137–140. https://doi.org/10.1038/ngeo419

Kagan, Y., & Knopoff, L. (1980). Dependence of seismicity on depth. *Bulletin of the Seismological Society of America*, *70*(5), 1811–1822.

Kameyama, M., Yuen, D. A., & Fujimoto, H. (1997). The interaction of viscous heating with grain-size dependent rheology in the formation of localized slip zones. *Geophysical Research Letters*, *24*(20), 2523–2526. https://doi.org/10.1029/97gl02648

Kameyama, M., Yuen, D. A., & Karato, S.-I. (1999). Thermal-mechanical effects of low-temperature plasticity (the Peierls mechanism) on the deformation of a viscoelastic shear zone. *Earth and Planetary Science Letters*, *168*(1–2), 159–172. https://doi.org/10.1016/s0012-821x(99)00040-0

Kanamori, H., Anderson, D. L., & Heaton, T. H. (1998). Frictional melting during the rupture of the 1994 Bolivian earthquake. *Science*, *279*(5352), 839–842. https://doi.org/10.1126/science.279.5352.839

Karato, S.-i., Riedel, M. R., & Yuen, D. A. (2001). Rheological structure and deformation of subducted slabs in the mantle transition zone: Implications for mantle circulation and deep earthquakes. *Physics of the Earth and Planetary Interiors*, *127*(1–4), 83–108. https://doi.org/10.1016/s0031-9201(01)00223-0

Kaus, B. J. P., de Montserrat, A., Medinger, N., Riel, N., Cosarinky, M., Berlie, N., et al. (2023). JuliaGeodynamics/GeoParams.jl: v0.5.1 [Software]. *Zenodo*. https://doi.org/10.5281/zenodo.10050339

Kaus, B. J. P., & Podladchikov, Y. Y. (2006). Initiation of localized shear zones in viscoelastoplastic rocks. *Journal of Geophysical Research*, *111*(B4). https://doi.org/10.1029/2005jb003652

Kawazoe, T., Karato, S.-i., Otsuka, K., Jing, Z., & Mookherjee, M. (2009). Shear deformation of dry polycrystalline olivine under deep upper mantle conditions using a rotational Drickamer apparatus (RDA). *Physics of the Earth and Planetary Interiors*, *174*(1–4), 128–137. https://doi.org/10.1016/j.pepi.2008.06.027

Kelemen, P. B., & Hirth, G. (2007). A periodic shear-heating mechanism for intermediate-depth earthquakes in the mantle. *Nature*, *446*(7137), 787–790. https://doi.org/10.1038/nature05717

Kirby, S. H. (1987). Localized polymorphic phase transformations in high-pressure faults and applications to the physical mechanism of deep earthquakes. *Journal of Geophysical Research*, *92*(B13), 13789–13800. https://doi.org/10.1029/jb092ib13p13789

Kirby, S. H., Stein, S., Okal, E. A., & Rubie, D. C. (1996). Metastable mantle phase transformations and deep earthquakes in subducting oceanic lithosphere. *Reviews of Geophysics*, *34*(2), 261–306. https://doi.org/10.1029/96rg01050

Kiss, D., Moulas, E., Kaus, B. J. P., & Spang, A. (2023). Decompression and fracturing caused by magnetically induced thermal stresses. *Journal of Geophysical Research: Solid Earth*, *128*(3), e2022JB025341. https://doi.org/10.1029/2022jb025341

Kiss, D., Podladchikov, Y. Y., Duretz, T., & Schmalholz, S. M. (2019). Spontaneous generation of ductile shear zones by thermal softening: Localization criterion, 1D to 3D modelling and application to the lithosphere. *Earth and Planetary Science Letters*, *519*, 284–296. https://doi.org/10.1016/j.epsl.2019.05.026

Kumamoto, K. M., Thom, C. A., Wallis, D., Hansen, L. N., Armstrong, D. E., Warren, J. M., et al. (2017). Size effects resolve discrepancies in 40 years of work on low-temperature plasticity in olivine. *Science Advances*, *3*(9), e1701338. https://doi.org/10.1126/sciadv.1701338

Leith, A., & Sharpe, J. (1936). Deep-focus earthquakes and their geological significance. *The Journal of Geology*, *44*(8), 877–917. https://doi.org/10.1086/624495

Leloup, P. H., Ricard, Y., Battaglia, J., & Lacassin, R. (1999). Shear heating in continental strike-slip shear zones: Model and field examples. *Geophysical Journal International*, *136*(1), 19–40. https://doi.org/10.1046/j.1365-246x.1999.00683.x

Li, M., Pranger, C., & van Dinther, Y. (2022). Characteristics of earthquake cycles: A cross-dimensional comparison of 0D to 3D numerical models. *Journal of Geophysical Research: Solid Earth*, *127*(8), e2021JB023726. https://doi.org/10.1029/2021jb023726

Li, Z.-H., Gerya, T., & Connolly, J. A. (2019). Variability of subducting slab morphologies in the mantle transition zone: Insight from petrological-thermomechanical modeling. *Earth-Science Reviews*, *196*, 102874. https://doi.org/10.1016/j.earscirev.2019.05.018

Liu, M., Kerschhofer, L., Mosenfelder, J. L., & Rubie, D. C. (1998). The effect of strain energy on growth rates during the olivine-spinel transformation and implications for olivine metastability in subducting slabs. *Journal of Geophysical Research*, *103*(B10), 23897–23909. https://doi.org/10.1029/98jb00794

McGuire, J. J., Wiens, D. A., Shore, P. J., & Bevis, M. G. (1997). The March 9, 1994 (M w 7.6), deep Tonga earthquake: Rupture outside the seismically active slab. *Journal of Geophysical Research*, *102*(B7), 15163–15182. https://doi.org/10.1029/96jb03185

Meade, C., & Jeanloz, R. (1991). Deep-focus earthquakes and recycling of water into the Earth's mantle. *Science*, *252*(5002), 68–72. https://doi.org/10.1126/science.252.5002.68

Mulyukova, E., & Bercovici, D. (2017). Formation of lithospheric shear zones: Effect of temperature on two-phase grain damage. *Physics of the Earth and Planetary Interiors*, *270*, 195–212. https://doi.org/10.1016/j.pepi.2017.07.011

Ogawa, M. (1987). Shear instability in a viscoelastic material as the cause of deep focus earthquakes. *Journal of Geophysical Research*, *92*(B13), 13801–13810. https://doi.org/10.1029/jb092ib13p13801

Ohuchi, T., Lei, X., Ohfuji, H., Higo, Y., Tange, Y., Sakai, T., et al. (2017). Intermediate-depth earthquakes linked to localized heating in dunite and harzburgite. *Nature Geoscience*, *10*(10), 771–776. https://doi.org/10.1038/ngeo3011

Piccolo, A., Palin, R. M., Kaus, B. J. P., & White, R. W. (2019). Generation of Earth's early continents from a relatively cool Archean mantle. *Geochemistry, Geophysics, Geosystems*, *20*(4), 1679–1697. https://doi.org/10.1029/2018gc008079

Pranger, C., Sanan, P., May, D. A., Le Pourhiet, L., & Gabriel, A.-A. (2022). Rate and state friction as a spatially regularized transient viscous flow law. *Journal of Geophysical Research: Solid Earth*, *127*(6), e2021JB023511. https://doi.org/10.1029/2021jb023511

Prieto, G. A., Florez, M., Barrett, S. A., Beroza, G. C., Pedraza, P., Blanco, J. F., & Poveda, E. (2013). Seismic evidence for thermal runaway during intermediate-depth earthquake rupture. *Geophysical Research Letters*, *40*(23), 6064–6068. https://doi.org/10.1002/2013gl058109

Raleigh, C., & Paterson, M. (1965). Experimental deformation of serpentinite and its tectonic implications. *Journal of Geophysical Research*, *70*(16), 3965–3985. https://doi.org/10.1029/jz070i016p03965

Räss, L., Utkin, I., Duretz, T., Omlin, S., & Podladchikov, Y. Y. (2022). Assessing the robustness and scalability of the accelerated pseudo-transient method. *Geoscientific Model Development*, *15*(14), 5757–5786. https://doi.org/10.5194/gmd-15-5757-2022

Regenauer-Lieb, K., & Yuen, D. (2003). Modeling shear zones in geological and planetary sciences: Solid-and fluid-thermal–mechanical approaches. *Earth-Science Reviews*, *63*(3–4), 295–349. https://doi.org/10.1016/s0012-8252(03)00038-2

Regenauer-Lieb, K., & Yuen, D. (2004). Positive feedback of interacting ductile faults from coupling of equation of state, rheology and thermal-mechanics. *Physics of the Earth and Planetary Interiors*, *142*(1–2), 113–135. https://doi.org/10.1016/j.pepi.2004.01.003

Regenauer-Lieb, K., & Yuen, D. A. (1998). Rapid conversion of elastic energy into plastic shear heating during incipient necking of the lithosphere. *Geophysical Research Letters*, *25*(14), 2737–2740. https://doi.org/10.1029/98gl02056

Renshaw, C. E., & Schulson, E. M. (2007). Limits on rock strength under high confinement. *Earth and Planetary Science Letters*, *258*(1–2), 307–314. https://doi.org/10.1016/j.epsl.2007.03.043

Ricard, Y., & Bercovici, D. (2009). A continuum theory of grain size evolution and damage. *Journal of Geophysical Research*, *114*(B1). https://doi.org/10.1029/2007jb005491

Rozel, A., Ricard, Y., & Bercovici, D. (2011). A thermodynamically self-consistent damage equation for grain size evolution during dynamic recrystallization. *Geophysical Journal International*, *184*(2), 719–728. https://doi.org/10.1111/j.1365-246x.2010.04875.x

Ruh, J. B., Tokle, L., & Behr, W. M. (2022). Grain-size-evolution controls on lithospheric weakening during continental rifting. *Nature Geoscience*, *15*(7), 585–590. https://doi.org/10.1038/s41561-022-00964-9

Schmalholz, S., & Duretz, T. (2015). Shear zone and nappe formation by thermal softening, related stress and temperature evolution, and application to the Alps. *Journal of Metamorphic Geology*, *33*(8), 887–908. https://doi.org/10.1111/jmg.12137

Schubnel, A., Brunet, F., Hilairet, N., Gasc, J., Wang, Y., & Green, H. W. (2013). Deep-focus earthquake analogs recorded at high pressure and temperature in the laboratory. *Science*, *341*(6152), 1377–1380. https://doi.org/10.1126/science.1240206

Spang, A., Thielmann, M., & Kiss, D. (2024). Numerical model used in "Rapid ductile strain localization due to thermal runaway" [Software]. *Zenodo*. https://doi.org/10.5281/zenodo.12167393

Spray, J. G. (1995). Pseudotachylyte controversy: Fact or friction? *Geology*, *23*(12), 1119–1122. https://doi.org/10.1130/0091-7613(1995)023<1119:pcfof>2.3.co;2

Thielmann, M. (2018). Grain size assisted thermal runaway as a nucleation mechanism for continental mantle earthquakes: Impact of complex rheologies. *Tectonophysics*, *746*, 611–623. https://doi.org/10.1016/j.tecto.2017.08.038

Thielmann, M., & Kaus, B. J. (2012). Shear heating induced lithospheric-scale localization: Does it result in subduction? *Earth and Planetary Science Letters*, *359*, 1–13. https://doi.org/10.1016/j.epsl.2012.10.002

Thielmann, M., Rozel, A., Kaus, B. J. P., & Ricard, Y. (2015). Intermediate-depth earthquake generation and shear zone formation caused by grain size reduction and shear heating. *Geology*, *43*(9), 791–794. https://doi.org/10.1130/g36864.1

Tibi, R., Bock, G., & Wiens, D. A. (2003). Source characteristics of large deep earthquakes: Constraint on the faulting mechanism at great depths. *Journal of Geophysical Research*, *108*(B2). https://doi.org/10.1029/2002jb001948

Tingle, T. N., Green II, H. W., Scholz, C. H., & Koczynski, T. (1993). The rheology of faults triggered by the olivine-spinel transformation in Mg_2GeO_4 and its implications for the mechanism of deep-focus earthquakes. *Journal of Structural Geology*, *15*(9–10), 1249–1256. https://doi.org/10.1016/0191-8141(93)90167-9

Toffol, G., Yang, J., Pennacchioni, G., Faccenda, M., & Scambelluri, M. (2022). How to quake a subducting dry slab at intermediate depths: Inferences from numerical modelling. *Earth and Planetary Science Letters*, *578*, 117289. https://doi.org/10.1016/j.epsl.2021.117289

Tresca, M. H. (1878). On further applications of the flow of solids. *Proceedings - Institution of Mechanical Engineers*, *29*(1), 301–345. https://doi.org/10.1243/pime_proc_1878_029_017_02

Turner, H. (1922). On the arrival of earthquake waves at the antipodes, and on the measurement of the focal depth of an earthquake. *Geophysical Journal International*, *1*, 1–13. https://doi.org/10.1111/j.1365-246x.1922.tb05354.x

Venkataraman, A., & Kanamori, H. (2004). Observational constraints on the fracture energy of subduction zone earthquakes. *Journal of Geophysical Research*, *109*(B5). https://doi.org/10.1029/2003jb002549

Wadati, K. (1928). Shallow and deep earthquakes. *Geophysical Magazine*, *1*, 162–202.

Wang, Y., Zhu, L., Shi, F., Schubnel, A., Hilairet, N., Yu, T., et al. (2017). A laboratory nanoseismological study on deep-focus earthquake micromechanics. *Science Advances*, *3*(7), e1601896. https://doi.org/10.1126/sciadv.1601896

Ye, L., Lay, T., Kanamori, H., Zhan, Z., & Duputel, Z. (2016). Diverse rupture processes in the 2015 Peru deep earthquake doublet. *Science Advances*, *2*(6), e1600581. https://doi.org/10.1126/sciadv.1600581

Yuen, D. A., Fleitout, L., Schubert, G., & Froidevaux, C. (1978). Shear deformation zones along major transform faults and subducting slabs. *Geophysical Journal International*, *54*(1), 93–119. https://doi.org/10.1111/j.1365-246x.1978.tb06758.x

Zhan, Z. (2017). Gutenberg–Richter law for deep earthquakes revisited: A dual-mechanism hypothesis. *Earth and Planetary Science Letters*, *461*, 1–7. https://doi.org/10.1016/j.epsl.2016.12.030

Zhan, Z. (2020). Mechanisms and implications of deep earthquakes. *Annual Review of Earth and Planetary Sciences*, *48*(1), 147–174. https://doi.org/10.1146/annurev-earth-053018-060314